

Transparency of 2 μm window of Titan's atmosphere

Pascal Rannou^{a,*}, Benoît Seignovert^a, S. Le Mouélic^b, L. Maltagliati^c, M. Rey^a, C. Sotin^d

^a*GSMA, Université de Reims Champagne-Ardenne, UMR 7331-GSMA, 51687 Reims, France*

^b*LPGN, UMR CNRS 6112, Université de Nantes, Nantes, France*

^c*Nature Publishing Group, London, United-Kingdom*

^d*Jet Propulsion Laboratory, California Institute of Technology, Pasadena, CA 91109, USA*

Abstract

Titan's atmosphere is optically thick and hides the surface and the lower layers from the view at almost all wavelengths. However, because gaseous absorptions are spectrally selective, some narrow spectral intervals are relatively transparent and allow to probe the surface. To use these intervals (called windows) a good knowledge of atmospheric absorption is necessary. Once gas spectroscopic linelists are well established, the absorption inside windows depends on the way the far wings of the methane absorption lines are cut-off. We know that the intensity in all the windows can be explained with the same cut-off parameters, except for the window at 2 μm . This discrepancy is generally treated with a workaround which consists in using a different cut-off description for this specific window. This window is relatively transparent and surface may have specific spectral signatures that could be detected. Thus, a good knowledge of atmosphere opacities is essential and our scope is to better understand what causes the difference between the 2 μm window and the other windows. In this work, we used scattered light at the limb and transmissions in occultation observed with VIMS (Visual Infrared Mapping Spectrometer) onboard Cassini, around the 2 μm window. Data shows an absorption feature that participates to the shape of this window. Our atmospheric model fits well the VIMS data at 2 μm with the same cut-off than for the other windows, provided an additional absorption is introduced in the middle of the window around $\sim 2.065 \mu\text{m}$. It explains well the discrepancy between the cut-off used at 2 μm , and we show that a gas with a fairly constant mixing ratio, possibly ethane, may be the cause of this absorption. Finally, we studied the impact of this absorption on the retrieval of the surface reflectivity and found that it is significant.

Keywords: Titan, Atmosphere

DOI: [10.1016/j.pss.2017.11.015](https://doi.org/10.1016/j.pss.2017.11.015)

1. Introduction

Titan, the largest satellite of Saturn, has a dense atmosphere of 1.44 bar and a thick haze layer of photochemical aerosols which hides the lower layers and the surface from view. Before the arrival of Cassini, the surface could be probed in near infrared by HST (Smith et al., 1996) and with ground based telescope thanks to the progress of adaptive optics (e.g., Combes et al., 1997; Coustenis et al., 2001; Hirtzig et al., 2005). Spectroscopic observations and spectro-imaging observations were used to retrieve surface reflectivity (Griffith et al., 1991, 2003; Coustenis et al., 1995; Negrão et al., 2006, 2007) with the information available at that time concerning methane absorption. During the same period of time, clouds were observed first with telescope spectroscopic observations (Griffith et al., 1998, 2000) and then imaged (Brown et al., 2002; Roe et al., 2005; Hirtzig et al., 2009). In some cases, radiative transfer model were use to determine cloud properties.

Cassini observations allowed us to obtain spectroscopic observations on a broad spectral range, with a good spatial resolution. With the information collected by Huygens during its descent and thanks to the advance in the knowledge of methane spectroscopic data, it is now possible to much better constrain surface properties inside the methane window (e.g., Griffith et al., 2012; Hirtzig et al., 2013) and to retrieve cloud characteristics as drop size, cloud altitude and opacity (Griffith et al., 2005, 2006; Le Mouélic et al., 2012).

Concerning Titan, one important issue came out from these studies. As for all planetary cases, the spectroscopic linelists which describes the gas absorption is composed of lines which can be represented as Dirac functions. Each line must be convolved by a specific widening profile to account for collisional and Doppler widening. For atmospheric purpose, when data is given with a moderate spectral resolution as in this study, a Voigt profile can be used. Far from the center of the line, this function turns to a slowly decreasing Lorentzian function which must be modified to decrease faster. To do so, a cut-off function is applied given limit of $|\nu - \nu_0|$, as for instance an exponential

*Corresponding author

Email address: pascal.rannou@univ-reims.fr (Pascal Rannou)

decay ($\exp(-|\nu - \nu_0|/\gamma)$) or any other decreasing function, to the Voigt profile (e.g., de Bergh et al., 2012). Cut-off can be more sophisticated as for instance with two limits and two different decays (Hartmann et al., 2002) or different cut-off functions.

However, it appeared from studies of Titan photometry that the cut-off parameters which must be applied to the line profiles are different at $2\ \mu\text{m}$ window than at other wavelengths (Griffith et al., 2012; Hirtzig et al., 2013). This is especially apparent when probing thick clouds because, in this case, when the atmosphere is not correctly set, surface reflectivity can no longer compensate the errors to get the correct spectral shape of the window. So far, to overcome this difficulty, several works were performed assuming a special wing cut-off at $2\ \mu\text{m}$, different from the wing cut-off in all other windows. This is not satisfactory because no clear reasons are given to justify such a difference and, moreover, for other planets such an adaptation from window to window is not necessary (e.g., Sromovsky et al., 2012; Fedorova et al., 2015).

Defining clearly the opacity inside the windows is especially important to retrieve accurately the surface albedo. We can either retrieve a single value for each window or a small part of spectra inside wide windows (that is beyond $1.5\ \mu\text{m}$). Conclusions on the presence of water ice, the strength of its signatures, or signatures of other components may be drawn from analysis of small parts of surface spectra collected in near infrared windows (e.g., Griffith et al., 2003; Hirtzig et al., 2013; Solomonidou et al., 2016). The retrieved surface albedo and eventually its spectral shape is strongly dependent on the atmosphere opacities, including gas opacity and thus on the cut-off prescription (Negrão et al., 2006, 2007; Solomonidou et al., 2014). Although albedo inside windows have not been discussed yet in literature, probably because atmosphere opacity remains too uncertain, it worths mentioning that they can hold valuable information provided that the opacity of the atmosphere above is correctly set.

In this work, we specifically study the intensity of scattered light at the limb of Titan, in the stratosphere in the $2\ \mu\text{m}$ window. There, the intensity essentially depends on the aerosol haze and gas properties. Doing so, we avoid the influence of the surface reflectivity, which remains essentially unknown. Our goal is to determine the components which produce the shape of the $2\ \mu\text{m}$ window and to define the conditions that would allow to model this window with the same cut-off parameters than for the other windows.

2. Data and model

2.1. Description of the data

The data analyzed in this paper is a mosaic of cubes from V1545974724_1 to V1545983419_1 taken by VIMS during the T22 flyby the 22 December 2006. This image shows the polar region, a large polar cloud, and the atmosphere at the limb of Titan, with a view taken at

113° phase angle (Le Mouélic et al., 2012). Thanks to this specific acquisition mode, this image has a very high spatial resolution and it is the only VIMS image that enables us to extract detailed vertical profiles of scattered light at the limb. The spatial resolution of this image is about 20 km, that is half an atmosphere scale height. The data have been calibrated in I/F using the pipeline described in Barnes et al. (2007) and also labelled *RC17* in the description given in Clark et al. (2016)¹. We consider that the shift in VIMS channel wavelengths, estimated to be on the order of 2 nm at the time of the T22 observation, is negligible for our study. The *noodle* mode was used for this T22 observation. We reconstructed the corresponding 2D image (Figure 1) by concatenating the whole series of 395 individual 64×1 pixels cubes. The spectral interval probed by VIMS range from $\lambda = 0.3$ to $5.1\ \mu\text{m}$, with 352 channels. In the infrared part, observed with 256 channels from $\lambda = 0.88$ to $5.1\ \mu\text{m}$, the full width at half maximum of the channels is between 0.013 to $0.022\ \mu\text{m}$, thus the spectral resolution is between 120 and 180. For this limb observation, we ignore the wavelength shift of $2.5\ \text{nm}$ which was observed in the recording of data. In this work, we focus our attention on the radiance factor at the limb in the northern hemisphere.

Although the image seems to probe all the northern polar region, the latitude range at the limb is quite moderate, from 38°N to 55°N at the far edge of the light crescent (Figure 1). We then extract only one vertical profile as further as possible from the end of the crescent. This set of data is representative of this region of Titan. The part of limb in the southern hemisphere, in the left and lower corner of the image, only extends up to 195 km. This is not enough to perform a study. First, the properties upper part of the atmosphere participate to the scattered intensity at lower altitude. This information is missing in the data. Secondly, between 195 km and the lower level that can be studied with this technique, we would not be able to collect more than 3 of 4 points. This is not enough to study the scattering at the limb.

For each of the 256 VIMS channels, we consider radiance factors I/F by selecting pixels in the three columns at the left edge of the images. We then obtain vertical I/F profiles, around 40°N , with a spatial resolution of about 20 km (Figure 2). A typical I/F profile roughly follows a scale height from the top of the atmosphere down to a given level, corresponding to a critical value of the tangential optical depth. In this part of the profile, the total intensity depends on the integrated opacity along the line of sight and on the average properties of the atmosphere (single scattering albedo, phase function). The multiple scattering may also play a role in the final result. Beyond the critical tangential opacity, the profile becomes constant or decreases, depending on the actual geometry of the observation, and there, the data does not yield any

¹atmos.nmsu.edu/data_and_services/atmospheres_data/Cassini/logs/vims-radiometric-calibration-pds-2016-v1.20.pdf

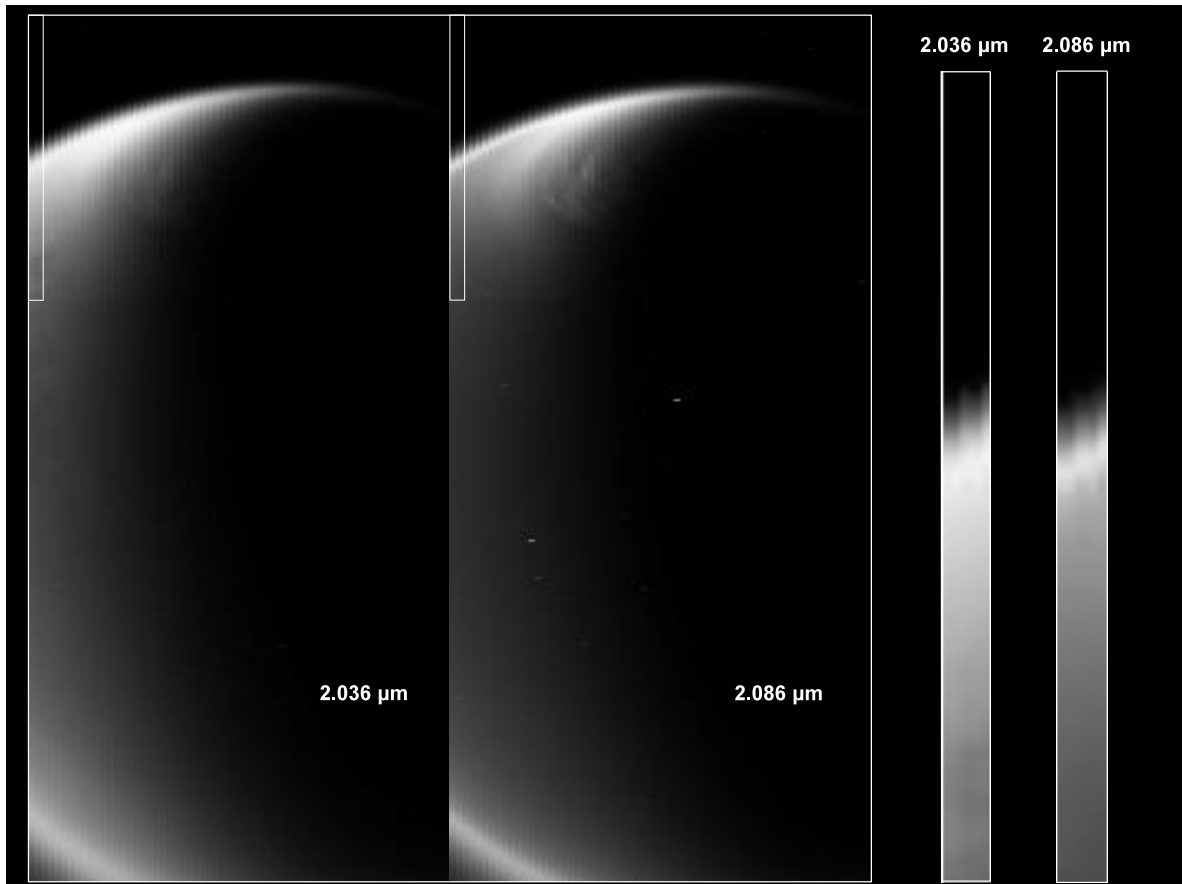


Fig. 1. Mosaic of VIMS images of Titan taken inside the methane 2 μ m window during the flyby T22, at two wavelengths (channels #167 and #170). For each wavelength, we used the pixels located in the three columns at the left hand side of the image, shown by the elongated rectangle. At the right side are shown a close up of the selected pixels at the same wavelengths.

more information about the atmosphere along all the line of sight. To study the atmosphere, we essentially consider the part of the profile which follows the scale height because it contains information about the vertical structure. Since haze opacity decreases with wavelength, VIMS is able to probe altitudes up to 500 km at 0.88 μ m and down to 50 km at 5 μ m. We therefore determine that the haze profile can be described with three different scale heights with transition around 225 km and 350 km (Figure 2).

On Titan, the observed radiance factors bear the spectral signature of methane which produces several alternate bands and windows. The outgoing intensity depends on the methane absorption and on the stratospheric haze. However, while the methane is the main source of opacity in the bands, it is less of a factor for the opacity in windows. As a consequence, the spectral shape of the radiance factor in windows depends on the gaseous continuum. The balance between the haze and methane extinction will be an important issue in our study of the 2 μ m windows.

Another important issue concerns the absorption by ethane which leaves a significant signature, as demonstrated with occultation observations by [Maltagliati et al. \(2015\)](#). Several unexplained absorption features appear well correlated to the ethane cross-section ([Sharpe et al.](#),

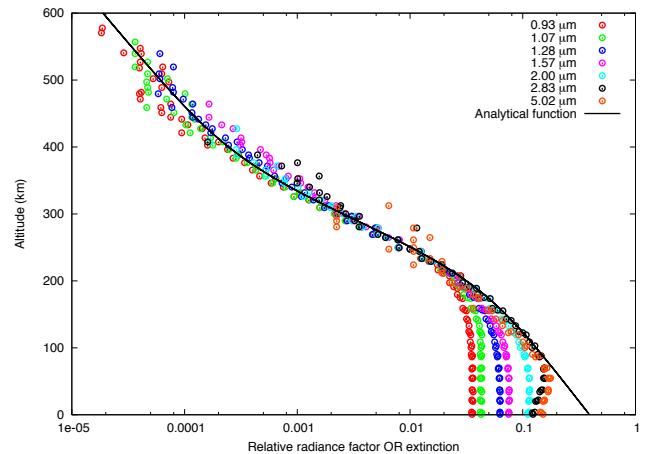


Fig. 2. Profiles of radiance factors observed inside the seven windows probed by VIMS-IR. Each point corresponds to the radiance factor of a pixel in the selected zone shown in the Figure 1. The continuous line shows the extinction profile from our model that best reproduces the radiance factor profiles. All profiles are scaled in this plot to obtain overlapping profiles. This comparison of scaled profiles makes visually appearing the vertical structure of the extinction profile down to 100 km, the altitude below which the profile at the most transparent wavelength (5.03 μ m) becomes saturated.

2004) measured at ambient temperature and standard pressure. However, it is not possible to perform a valuable analysis because these cross-sections are not suitable for use at all pressures or at the temperature range of Titan. No spectroscopic linelist yet exist in the wavelength range studied in this work. Therefore, to perform our analysis, we decided to remove the spectral intervals where ethane obviously participates to the absorption (Maltagliati et al., 2015), except in the core of the 2 μm window which is the scope of this study.

2.2. Description of the model

To perform this work, we used the model of scattering at the limb of a planet as described first in Rages et al. (1983), and used by Rannou et al. (1997, 2006). In this model, the calculation first consists in summing the single scattered intensity along a line of sight at the limb of the planet assuming a spherical geometry. This step es-

$$\rho_{ms}(z) = \frac{\int_0^\pi \int_0^{2\pi} I(\tau, \theta, \phi) \times P(\tau, \Theta_s[\theta_e, \phi_e, \theta, \phi]) d\Omega + F_0 \times \exp(-\tau/\mu_0) \times P(\tau, \Theta_s[\theta_e, \phi_e, \theta_0, \phi_0])}{F_0 \times \exp(-\tau/\mu_0) \times P(\tau, \Theta_s[\theta_e, \phi_e, \theta_0, \phi_0])} \quad (1)$$

where θ and ϕ indicate a direction of the space relative to the normal direction and relative to an arbitrary azimuth, θ_e and ϕ_e indicates the emergence direction (toward the observer), θ_0 and ϕ_0 is the incident direction of the solar photons, τ is the vertical optical depth of the altitude z (with a value set to 0 at the top of the atmosphere), $P(\tau, \Theta_s)$ is the phase function at the scattering angle Θ_s and at the level τ . $I(\tau, \theta, \phi)$ is the intensity field at the level τ and F_0 is the solar flux at Titan (Figure 3).

The integral term is positively-definite or null and it describes the integration of the scattered intensity converging toward one parcel of the atmosphere (this is the scattered part of the actinic flux). The term involving the solar flux F_0 is strictly positive and describes the direct solar photons. Thus, we see that in absence of scattered

essentially turns into computing the optical thickness and the Beer-Lambert attenuation along the incoming path of the solar photons and the outgoing path of the scattered photons to the probe. For this, we need to discretize the atmosphere in n layers, bounded by $n + 1$ levels. The atmosphere properties are supposed to be uniform inside a given layer. In this model, we used 70 layers of 10 km thickness.

In a second step, we evaluate the multiple scattering by using a model of atmosphere, whose properties are representative of Titan. This model evaluates at each level of the atmosphere the total amount of scattered photons toward the observer relatively to the direct photons from the sun scattered once toward the observer. This computation is performed with the relevant geometry for the incident flux and for the outgoing direction at the plane of the limb. We then obtain the multiple to single scattering ratio, $\rho_{ms}(z)$, as a function of the altitude (z), defined as:

photons ($I(\tau, \theta, \phi) = 0$), $\rho_{ms}(z)$ takes the lowest possible value, that is 1. As soon as there is a contribution of scattered light, $\rho_{ms}(z)$ increases and is boundless. Therefore, multiple scattering always increases the observed intensity relatively to single scattering. A value $\rho_{ms}(z) \gg 1$ indicates that the amount of scattered light largely exceeds the direct light from the Sun and the final intensity that is computed is dominated by multiple scattering.

This estimation, $\rho_{ms}(z)$, is then used as a multiplying factor for the singly scattered light by each volume of atmosphere along the line of sight. The final radiance factor I/F of the n^{th} layer (where $n=1$ is for the upper layer), integrated along a line of sight, is calculated following Rages et al. (1983) with the following equation:

$$I/F_n = \sum_{i=1}^{2n} \int_{x_{i-1}}^{x_i} \frac{\varpi_j P_j(\Theta_s)}{4} \exp(-\tau_i^0 - \tau_i^1) k(z(x)) \rho_{ms}(z(x)) dx \quad (2)$$

where the summation is performed on the $2 \times n$ segments which are defined by the intersections of the line of sight and the spherical shells defining the layers boundaries. Each layer of the atmosphere is crossed twice. The impact factor, that is the lowest altitude reached by the line of sight, is given by the bottom of the n^{th} layer. x is the abscissa along the line of sight. τ_i^0 and τ_i^1 are the opacities along the incident and emergent path. ϖ_j is the average single scattering of the layer j , where the index $j = i$ if $j < n + 1$ and $j = 2 \times n + 1 - i$ if $j > n$.

The multiple scattering factor $\rho_{ms}(z(x))$ is relevant only at the plane of the limb (that is for $x = 0$). However, we apply this factor everywhere, using the relevant altitude $z(x)$. To support this approximation, we evaluated that the contribution function along a line of sight is approximately a Gaussian function centered on $x = 0$ with a variance $\simeq \sqrt{(R_T + z_0) \times H}$, where R_T is the radius of Titan, z_0 is the impact parameter of the observation and H is the haze scale height. This variance is approximately 380 km. We estimate that, in order to account for

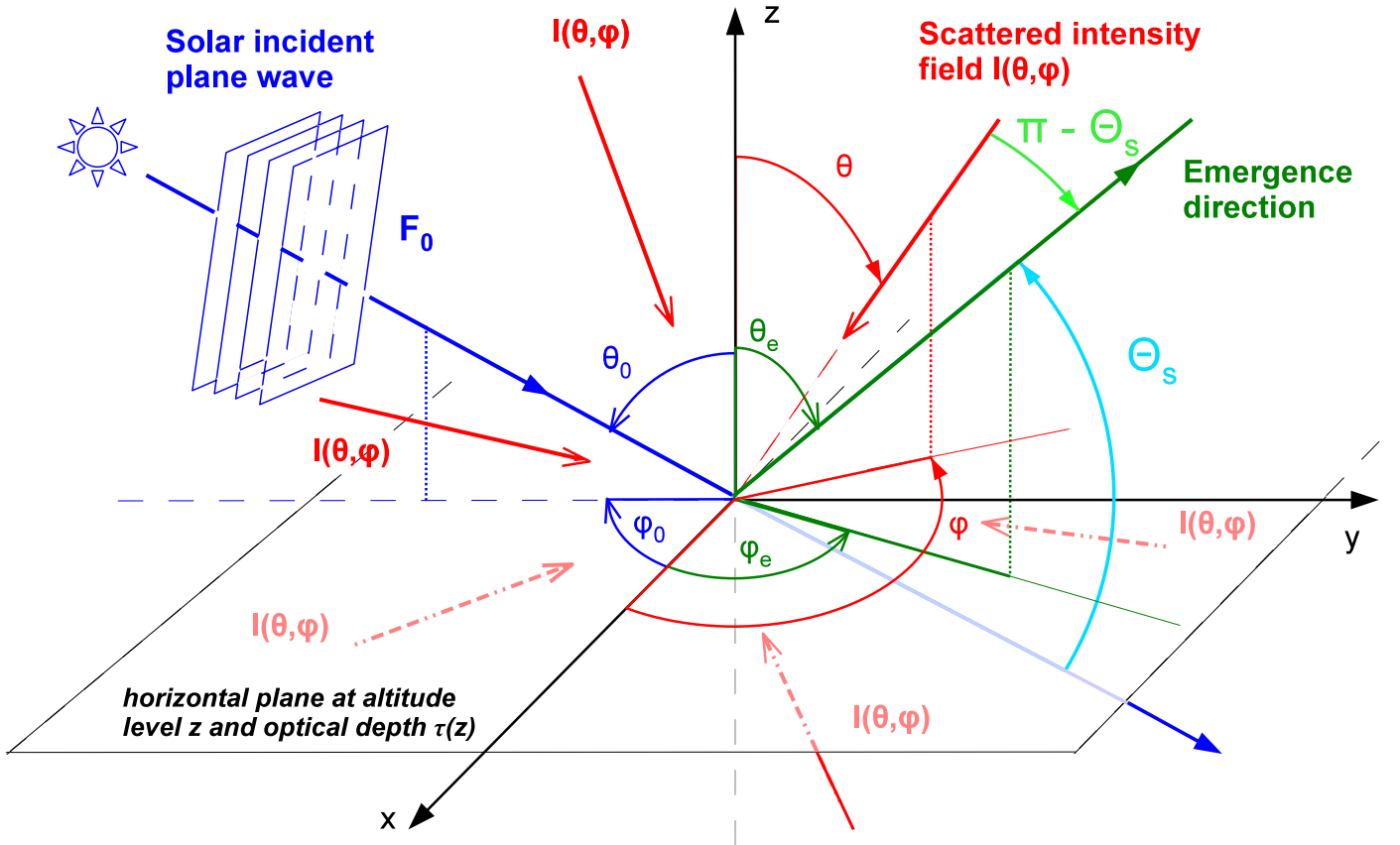


Fig. 3. Sketch displaying the geometry of the scattering at a given layer of the atmosphere for the direction of the incoming solar flux $F_0(\tau)$ (θ_0 and ϕ_0) (blue lines), the scattered intensity field $I(\tau, \theta, \phi)$ (red lines) and the emerging direction θ_e et ϕ_e (green). The scattering angle Θ_s between the solar incidence direction and the emergence direction ($\Theta_s(\theta_0, \phi_0, \theta_e, \phi_e)$), the supplementary angle (used for the clarity of the graph) of the scattering angle between a beam of the scattered field and the emergence direction is shown in light green.

the change in geometry along the line of sight, one should change the local incident angle by about $\pm 9^\circ$ around the reference value θ_0 (equal to 23° for this image). This gives a minor effect, first, because the incident angle is close to nadir so the multiple scattering only weakly depends on the incident angle. The value of ρ_{ms} changes by 0.38% per degree and then $\pm 3.4\%$ for $\pm 9^\circ$. Secondly, there is an anti-symmetrical effect for the variation of $\rho_{ms}(z)$ around the reference value calculated with positive and negative angular shift which cancels out the difference along the line of sight. We then finally used the value of $\rho_{ms}(z)$ calculated for the geometry at the limb for all the part of the line of sight.

2.3. Optical properties of aerosols

To account for haze properties, we followed the description given by Doose et al. (2016). Hereafter the terms *haze* and *aerosols* are used indifferently to designate the haze layer of photochemical aerosols and the aerosol particles. The phase functions that we used are therefore modified relatively to those published in Tomasko et al. (2008). For the other spectral properties, we use a model of scattering by fractal aggregates with optical constants

tuned to match the available constraints. We used the same aggregate characteristics as used by Doose et al. (2016) and Tomasko et al. (2008), that is aggregates with a fractal dimension $D_f = 2$ and with 3000 spherical grains (monomers) of 50 nm. We then seek the imaginary refractive index that allows us to match the single scattering albedo published by Doose et al. (2016) between 400 nm and 900 nm. The single scattering albedo of the photochemical haze above 80 km and the mist layer below 80 km are significantly different than those published by Tomasko et al. (2008), and thus we expect to see differences in the refractive indices of the aerosols. We used the same procedure as explained in Rannou et al. (2010). Once the particle geometry is defined, and assuming the real part of the refractive index from Khare et al. (1984), the imaginary part of the refractive index κ is the only parameter that remains to determine. Once retrieved, we use the refractive index to compute the extinction cross-sections σ_H and the single scattering albedo ϖ_H of the aerosols.

For this study, we leave the vertical structure of the haze as free parameters. I/F profiles at different wavelengths clearly show that three parameters X_1 , X_2 and X_3 can be used to describe the haze vertical profile above about

100 km (Figure 2). Below 80 km, we assume a layer of undefined material which has the same properties as defined in Doose et al. (2016) and Tomasko et al. (2008). Following de Bergh et al. (2012), we use the same phase function for the mist as for the haze, and we used the same relationship as in Doose et al. (2016) to fix the single scattering albedo of this layer, that is $\varpi_M = (0.565 + \varpi_H)/1.5$ while the spectral slope of the mist is the same as for the haze.

2.4. Choice of gas absorption linelist

The gas linelists that we used come from the Hitran database (Rothman et al., 2013) for all gases except for methane and its isotopes. The linelists for methane CH₄, deuterated methane CH₃D and the ¹³CH₄ are provided by Rey et al. (2013) from theoretical calculations. These linelists have been shown to give good results compared to the empirical band model of Karkoschka and Tomasko (2010), dedicated to match Titan photometry, and do not present any of the flaws that can be observed in Hitran or in Exomol databases (Rothman et al., 2013; Yurchenko and Tennyson, 2014). A thorough comparison is performed by Rey et al. (2017) to evaluate the value of different databases in the frame of Titan photometry.

When a spectroscopic linelist is used for atmospheric purposes, we have to convolve each line by a widening profile. We used a Voigt profile with a cut-off applied at $\Delta\nu_{co} = |\nu - \nu_0|$ from the center of the line ν_0 and a sublorentzian decay γ_{co} . We cut-off the Voigt profile by multiplying it by a function $\phi(\Delta\nu = |\nu - \nu_0|)$, where $\phi(\Delta\nu) = 1$ if $\Delta\nu < \Delta\nu_{co}$ and $\phi(\Delta\nu) = \phi_0 \times \exp(-\Delta\nu/\gamma_{co})$ if $\Delta\nu > \Delta\nu_{co}$ (de Bergh et al., 2012). ϕ_0 is set in order to ensure the continuity of the function $\phi(\Delta\nu)$. $\Delta\nu_{co}$ and γ_{co} are free parameters and they are the main focus of this work. We use as reference values for Titan $\Delta\nu_{co} = 26 \text{ cm}^{-1}$ and $\gamma_{co} = 120 \text{ cm}^{-1}$. This set up gives good match of the intensity at all windows except at 2 μm . We use the line broadening parameters for the Lorentzian profile $\alpha_0 = 6.5 \cdot 10^{-2}$ and the exponent $n = 0.85$, which are relevant for CH₄ in N₂ (Menard-Bourcin et al., 2007). All the other rules needed to build coefficients for the gas absorption from the linelists are defined without additional parameters (e.g., Hanel et al., 2003). The only other gaseous absorption which participates, marginally, to the outgoing intensity is provided by the pressure induced absorption of N₂-N₂ and N₂-H₂ dimers at 2 μm from McKellar (1989).

Pressure and temperature profiles needed to compute the gas opacities are those retrieved by the Huygens Atmospheric Structure Instrument (HASI) (Fulchignoni et al., 2005) while the methane mixing ratio comes from the latest analysis of the Gas Chromatograph Mass Spectrometer (GCMS) (Niemann et al., 2010). To treat the gaseous absorption in the radiative transfer model, we used the correlated-k method (Goody et al., 1989), and we used this method with 4 terms for each VIMS spectral channel (Rannou et al., 2010).

3. Study of the 2 μm window

Our computations are restricted to near the 2 μm window, between 1.75 and 2.40 μm . We exclude four spectral regions ([1.75-1.79 μm], [1.85-1.97 μm], [2.025-2.045 μm] and [2.15-2.40 μm]) from our analysis because they contain undetermined absorption features (Maltagliati et al., 2015). That leaves us with two intervals for our analysis: [1.79-1.85 μm] and [1.97-2.15 μm], from which we remove the channel #167. We also restrict the retrieval to the altitude range between 130 and 380 km. The upper and lower limits are defined respectively by the noise level and the level below which the I/F profile do no longer follow a scale height.

In the data, we readily see that a feature at 2.03 μm (channel #167), which is very sharp at high altitudes, smooths and widens with decreasing altitudes (Figure 4). This feature is located in the middle of the 2 μm window and apparently affect the atmosphere opacity as to produce the observed discrepancy in spectroscopic properties (Bailey et al., 2011; Griffith et al., 2012; Hirtzig et al., 2013). At lower altitude, we can see that I/F follows two different slopes, with an inflection around 2.03 μm . Even if we disregard the channel #167, this behaviour involves all the channels between 2 and 2.1 μm . Therefore, it can hardly be attributed to an instrumental effect. Such structure also appear in other images at much lower spatial resolution and with even more prominent signatures. Because this is inside a methane window, methane can not produce such an inflexion. Only a supplementary absorption can explain this. It shows that the 2 μm window is not smooth and featureless as generally thought and this features may also affect the spectra in close nadir viewing. Figure 5 displays the radiance factor obtained at the wavelength of the peak (channel #167, i.e. 2.036 μm) and in two surrounding channels. It shows a marked transition in the peak strength above 250 km, and the peak becomes very sharp above 300 km. It does not seem directly correlated to the haze structure. The relative difference of I/F between the channels #167 and the average of the surrounding channels (from #163 to #166 and from #168 to #170) quantifies the rapid change in the mesosphere, above 300 km. We checked if this peak is real or may be due to a problem in VIMS spectra. To do so, we sought for this peak elsewhere in the same VIMS image, especially in the terminator side where levels of intensity are similar to the limb. When mapping the peak signature, as for instance the intensity relative differences as plotted in Figure 5, we clearly observe discontinuities linked to the composite nature of the image. These discontinuities come from the image in the channel #167 and are not observed in other channels. This may have an instrumental origin linked to different sequences of observations. Although the peak itself may be real, we do not account for it in our analysis.

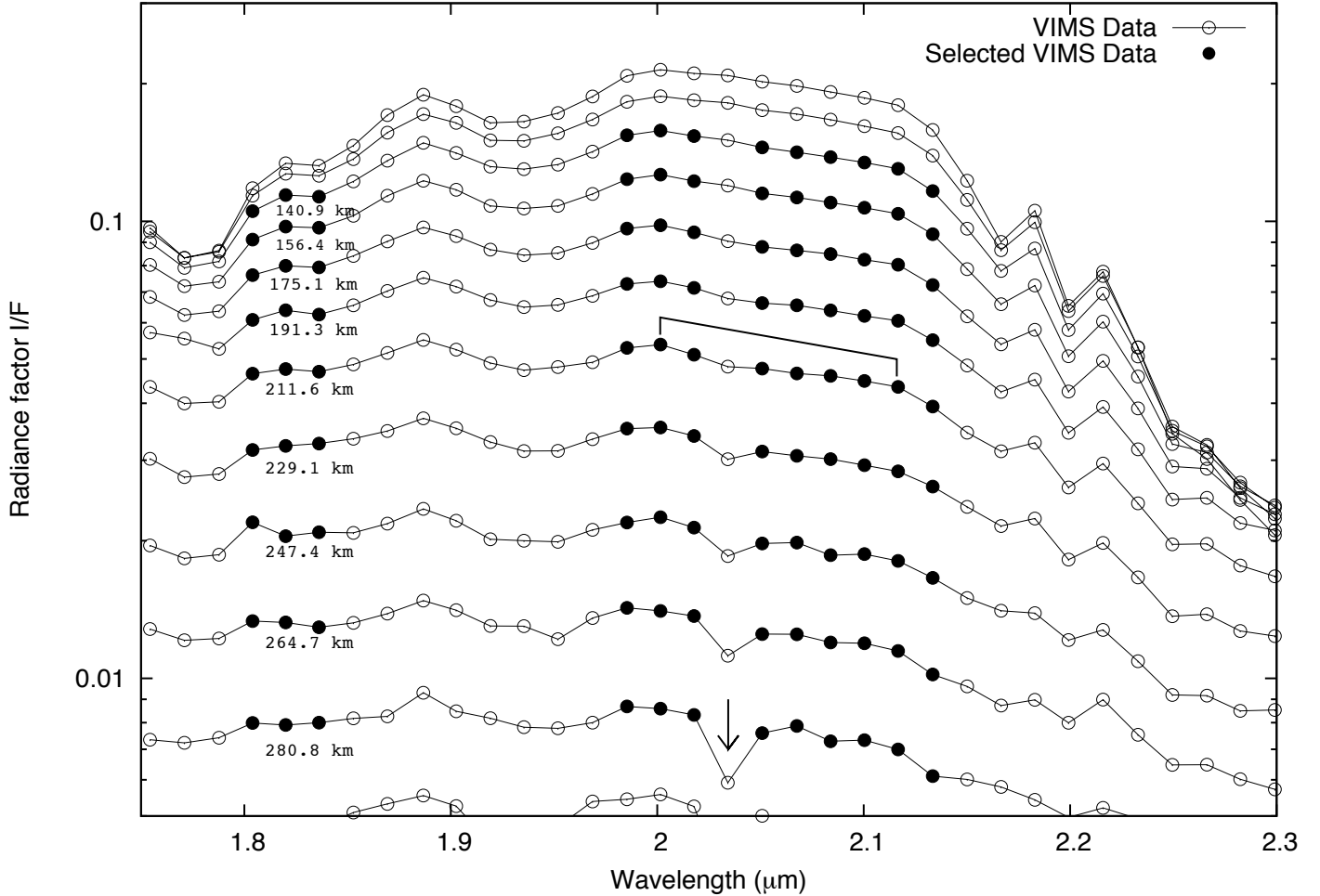


Fig. 4. Spectral variation of the radiance factors at several altitudes observed by VIMS. We removed from our analysis the major ethane absorption wavelengths and we remove altitudes where data are too noisy (above 300 km) and where the I/F profile becomes saturated (below 130 km) (empty circles). Only the data shown with filled circles are actually used in our analysis and for the retrievals. The spectra we used are labelled with their altitudes, from 140 km to 280 km. The vertical arrow shows the wavelength corresponding to channel #167, and the the bracket above the spectra at 211.6 km shows the spectral region where an additional absorption is needed, in the middle of the 2 μ m window. The uncertainty on the radiance factor ($\pm 3\%$) is comparable to the size of the symbols (Sromovsky et al., 2012).

3.1. Shape of the window

In this first step, our purpose is to use a model where haze and gases are treated in an usual manner, as described previously, in order to study the impact of line profile cut-off characteristics (i.e., $\Delta\nu_{co}$ and γ_{co}). Here the shape of the window is only a consequence of the haze properties and the gas extinction. In windows, the latter is controlled by the cut-off values. In this study, we also have to characterize the vertical profile of the haze extinc-

tion. There are three parameters for the vertical profile, X_1, X_2, X_3 , for the altitude regions below 225 km, between 225 and 350 km and above 350 km (Figure 2) and a fourth parameters to scale the amount of haze F_H . We note here that the parameters X_i do not strictly correspond to the scale height except for the two limiting behaviours ($z \rightarrow 0$ and $z \rightarrow \infty$). We define an analytical function to model the haze vertical profile with the following expression for the extinction:

$$k(z, \lambda) = A F_H \tau_{ref}(\lambda_0) \frac{\sigma_{ext}(\lambda)}{\sigma_{ext}(\lambda_0)} \times \left[\left(\frac{1}{\exp(-(z - z_1)/X_1)} + \frac{1}{\exp(-(z - z_1)/X_2)} \right)^{-1} + \left(\frac{1}{\exp(-(z_2 - z_1)/X_1)} + \frac{1}{\exp(-(z_2 - z_1)/X_2)} \right)^{-1} \times \exp(-(z - z_2)/X_3) \right] \quad (3)$$

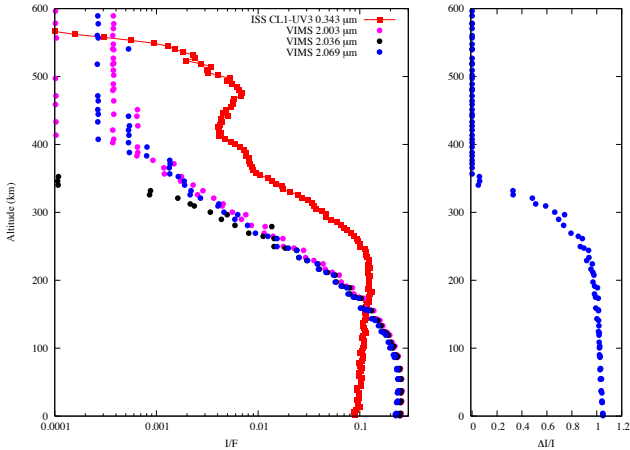


Fig. 5. At left: Profiles of radiance factor profile at 2.03 μm (channel #167) and at two surrounding wavelengths. The I/F profile decreases faster at 2.03 μm than in the two other profiles above 220 km thus showing the distribution of the peak. There is no apparent correlation with the haze distribution, shown with the I/F profile at 0.343 μm from the Cassini Imaging and Science Subsystem (ISS). At right: Relative strength of the peak computed as $\Delta I/I = (I/F_{167} - \langle I/F \rangle) / \langle I/F \rangle$ where $\langle I/F \rangle$ is a average value of I/F over the 6 channels from #164 to #170, excepted #167.

where $z_1 = 225$ km and $z_2 = 350$ km, $\tau_{ref}(\lambda_0)$ is the reference column opacity at $\lambda_0 = 1$ μm taken from Doose et al. (2016), $\sigma_{ext}(\lambda)$ is the aerosol cross-section as a function of the wavelength used for this work and A is the normalization factor of the expression between the brackets, integrated up $z = 55$ km to space. With this definition, F_H is simply a scaling factor for the column opacity of haze relatively to the value published by Doose et al. (2016), but the vertical distribution is controlled by the analytical function involving the parameters X_i and the spectral variation is given by the model of scattering by fractal aggregates and the new optical constants, as defined previously. Below $z = 55$ km, the layer has a constant extinction and is normalized with the prescription from Doose et al. (2016) as well. Two supplementary parameters concern the methane absorption (the cut-off parameters $\Delta\nu_{co}$ and γ_{co}). The other properties related to haze (cross-sections, phase function) and gaseous absorption are defined in the previous section. We then define the main structure of the haze profile by seeking, for each set of $\Delta\nu_{co}$ and γ_{co} , the set of parameters X_1 , X_2 , X_3 and F_H which best fit the I/F spectra. We use a Levenberg-Marquardt routine to minimize the χ^2 , and then we are also able to evaluate the quality of the solution. The shape of the analytical vertical profile of the extinction (Eq. 3) is not able to follow accurately all the small scale structures that may be in the real profile. Thus, to compute the χ^2 , we allow a scaling of the model intensity by less than 5% to minimize the differences between the model and the data at each level. Doing that, we assume that the real extinction profile may indeed have oscillations around the ideal guess which is displayed in Equation 3, and account for them.

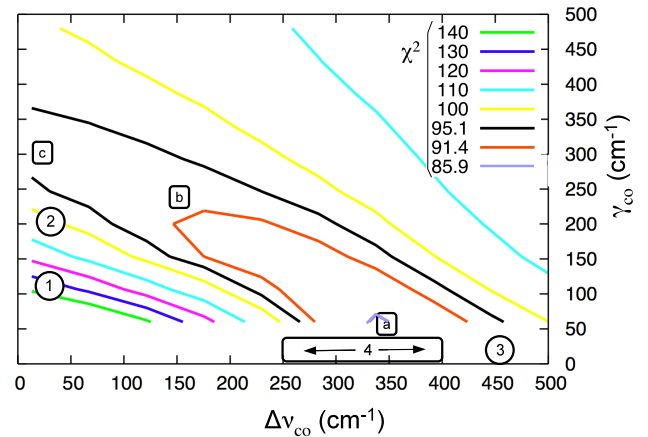


Fig. 6. Map of the χ^2 as a function of $\Delta\nu_{co}$ and γ_{co} , where χ^2 is defined as $\sum_{i=1}^N \frac{(I/F_{model} - I/F_{data})^2}{(\Delta I/F)^2}$ and $\Delta I/F_{data}$, the uncertainty on data is set as $0.03 \times I/F_{data}$ (after Sromovsky et al., 2012). The minimum value is around $\Delta\nu_{co} = 350$ cm^{-1} and $\gamma_{co} = 50$ cm^{-1} (label **a**). The value domain inside the 1 - σ and 2 - σ error are shown by the second contour ($\chi^2 = 91.4$ - orange) and third contour ($\chi^2 = 95.1$ - black). The χ^2 obtained using reference values for the cut-off (de Bergh et al., 2012, shown by the encircled 1) is clearly outside the zone of the minimum χ^2 . On the other hand, cut-off parameters found in other works (2 Hirtzig et al. (2013), 3 Griffith et al. (2012) and 4 Bailey et al. (2011)) are more consistent with the zone of minimum χ^2 . Values $(\Delta\nu_{co}, \gamma_{co})$ labelled **a**, **b** and **c** are used in the following as representative parameters for the region of minimum χ^2 .

Our results show that we are able to find a common vertical structure whatever the profile cut-off parameters. The results obtained with 72 sets of $(\Delta\nu_{co}, \gamma_{co})$ yield $F_h = 2.2805 \pm 0.0888$, $X_2 = 98.001 \pm 1.519$ km, $X_1 = 27.236 \pm 0.073$ km and $X_3 = 86.632 \pm 0.853$ km, where the uncertainties are given to 1 - σ . The best profile, with the lowest χ^2 , is displayed in Figure 2 (curve labelled *analytical function*). The uncertainty on X_2 is extremely small because this parameter is related to the part of the atmosphere between 225 and 350 km, in the middle of the altitude range, where the radiance factor follows a scale height. This vertical profile is quite similar to those reported ($H \simeq 60$ to 69 km between 140 and 176 km altitude and $H \simeq 45$ km between 176 and 278 km) by Vinatier et al. (2010) in far infrared (7.04 to 16.66 μm), at the same latitude (43.5°N and 46.5°N) and about the same period of the year (flyby T16, July 2006).

As for previous works (Bailey et al., 2011; Griffith et al., 2012; Hirtzig et al., 2013) we find that the 2 μm window is best fit with a cut-off applied further from the line center than the reference cut-off (Figure 6). The best results are obtained for values of $\Delta\nu_{co}$ and γ_{co} along the line defined by the points $(\Delta\nu_{co} = 50$ cm^{-1} , $\gamma_{co} = 350$ cm^{-1}) and $(\Delta\nu_{co} = 350$ cm^{-1} , $\gamma_{co} = 50$ cm^{-1}). In the following, we will refer to the cut-off parameters along this line as *extended cut-off parameters*. There, the reduced χ^2 values are around 0.85 (with the number of data minus parameters equal to $N - P = 103$). For the reference value

$\Delta\nu_{co} = 26 \text{ cm}^{-1}$ and $\gamma_{co} = 120 \text{ cm}^{-1}$, the reduced χ^2 is significantly larger, around 1.3. The exact values of these χ^2 and reduced χ^2 depends upon our knowledge of data uncertainties which is not well defined (Sromovsky et al., 2012). The comparison between the data and the model for selected values of $\Delta\nu_{co}$ and γ_{co} shows that the shape of the window is flatter and much better modelled with extended cut-off relatively to the reference choice (Figure 7). The parameters of the cut-off published previously are shown on the χ^2 map. They all show the same trend : the 2 μm -window is best fit with an extended cut-off, and there are several ways to extend the cut-off.

3.2. Absorption in the center the 2 μm window

As mentioned previously, there is a marked absorption in the centre of the 2 μm window below 300 km (Figure 4). To perform our analysis, we exclude the channel (#167) which potentially produces spurious values. Without this sharp peak, it still remains a broad and smooth absorption feature which is not accounted for by our model. Our scope in this part is to check the impact of this feature on the model results. In particular, we want to know if adding an absorption can improve the results and make other choices of $\Delta\nu_{co}$ and γ_{co} acceptable. The nature of this absorption feature is not known, and it may be produced by an absorption due to haze optical properties or it could be due to a gaseous species which may condense at the troposphere. From these hypotheses, we define three cases to include an absorption (Table 1).

For the first case (#1), we assume an absorption due to the haze layer by adding a Gaussian peak in aerosol absorption. We then add, for instance, $\Delta\sigma_{abs}(\lambda)$ to the absorption cross-section. It produces a corresponding increase in extinction ($\sigma'_{ext}(\lambda) = [\sigma_{abs}(\lambda) + \Delta\sigma_{abs}(\lambda)] + \sigma_{sca}(\lambda) = \sigma_{ext}(\lambda) + \Delta\sigma_{abs}(\lambda)$). The scattering properties are not modified, and to conserve the same scattering properties, the single scattering albedo must be modified as following: $\varpi'(\lambda) = \varpi(\lambda) \times \sigma_{ext}(\lambda) / \sigma'_{ext}(\lambda)$. To mimic an absorption peak due to aerosols, we use $\Delta\sigma_{abs}(\lambda) = \sigma_0 \times f(\lambda)$, where σ_0 is a reference cross-section and $f(\lambda)$ is the Gaussian form, defined as $f(\lambda) = A \exp(-(\lambda - \lambda_0)^2 / 2\Sigma^2)$, where the amplitude A , the peak wavelength λ_0 and standard deviation Σ can be left as free parameters.

In the second case (#2), we assume an absorption due to a gas with a constant mixing ratio. In this case, we add a contribution to the gaseous absorption by scaling it on the absorption per molecule computed for the methane. Notably, in windows, methane absorption is a smooth flat continuum. We then add a contribution $\Delta\tau_g(\lambda, i)$ to the gas opacity $\tau_g(\lambda, i)$ that is written as follow : $\Delta\tau_g(\lambda, i) = f(\lambda)n_g(z)b(z, \lambda, i)$ where z and i are, respectively, the altitude and the index of the terms for the correlated-k calculation ($i = 1, N$), $f(\lambda)$ is the form function, defined as previously, for the absorption peak, $n_g(z)$ is the total molecular concentration and $b(z, \lambda, i)$ the absorption coefficient of the methane used as reference

for this putative gas. Case #3 accounts for the absorption peak similar to the second way, except that the form function $f(\lambda)$ falls to zero below 60 km in order to mimic the effect of a sharp condensation in the lower stratosphere (Figure 8).

For all cases, we perform a new set of analysis to improve the fits. This time, for each values of $\Delta\nu_{co}$ and γ_{co} , we used the corresponding set of scale heights found previously for the haze, and no longer considered as free parameters. The amount of haze F_H is still considered as a free parameter as well as the three parameters of the Gaussian shape, A , λ_0 and Σ . We use again a Levenberg-Marquardt routine to find the best solution, and we first consider the χ^2 map for the three cases. For the three cases, we obtain similar results : if we add an absorption peak we are now able to obtain fits that have the same statistical significance (same values of χ^2) whatever the values $\Delta\nu_{co}$ and γ_{co} (Figure 9). This clearly means that any choice of parameters for the far wing cut-off can produce a valuable fit provided that an absorption feature is included. The χ^2 maps indicate that fits are slightly better, although not in a statistically significant way, for cut-off with small values of $\Delta\nu_{co}$ and γ_{co} , as for instance the reference values of de Bergh et al. (2012). This can also be seen on the fits of I/F spectra which are now very similar for any values of the parameters (Figure 10). Consequently, we conclude that the apparent discrepancy between the parameters of the far wing cut-off in different windows may be due to this absorption feature inside the 2 μm window.

Although the χ^2 maps appear smooth, we can see a dichotomy in the parameters of the Gaussian absorption peaks which produces the results (Figure 11). This occurs whatever the source of the absorption peak. Where the fit was the worse, at low values of $\Delta\nu_{co}$ and γ_{co} , we find that an absorption peak around $\lambda_0 \simeq 2.07$, with a dispersion around $\pm 0.02 \mu\text{m}$ significantly improves the fit. This occurs for parameters $\Delta\nu_{co}$ smaller than about 200 cm^{-1} and γ_{co} smaller than about 150 cm^{-1} . For larger values of $\Delta\nu_{co}$ and γ_{co} , the best fit is found with a peak beyond 2.10 cm^{-1} and this peak would reinforce the already existing absorption of the window side at long wavelengths (Figure 11). We excluded the range of wavelength beyond $2.10 \mu\text{m}$ that we attribute to ethane, and the supplementary absorption may possibly be a residual absorption by the far side of ethane band around $2.3 \mu\text{m}$. It is important however to note that results where the peak is located around $2.07 \mu\text{m}$ are significantly improved (in a statistical point of view) while results with a peak beyond $2.10 \mu\text{m}$ are only marginally improved, as it can be concluded from the χ^2 values. Notably, the new χ^2 values, obtained assuming an absorption peak, are very similar for the three cases, suggesting that they are equivalent despite corresponding to different ways to include the absorption.

3.3. Absorption peak at $\sim 2.07 \mu\text{m}$

We now focus on cases with a peak at $\lambda_0 < 2.10 \mu\text{m}$, which corresponds to an absorption in the centre of the

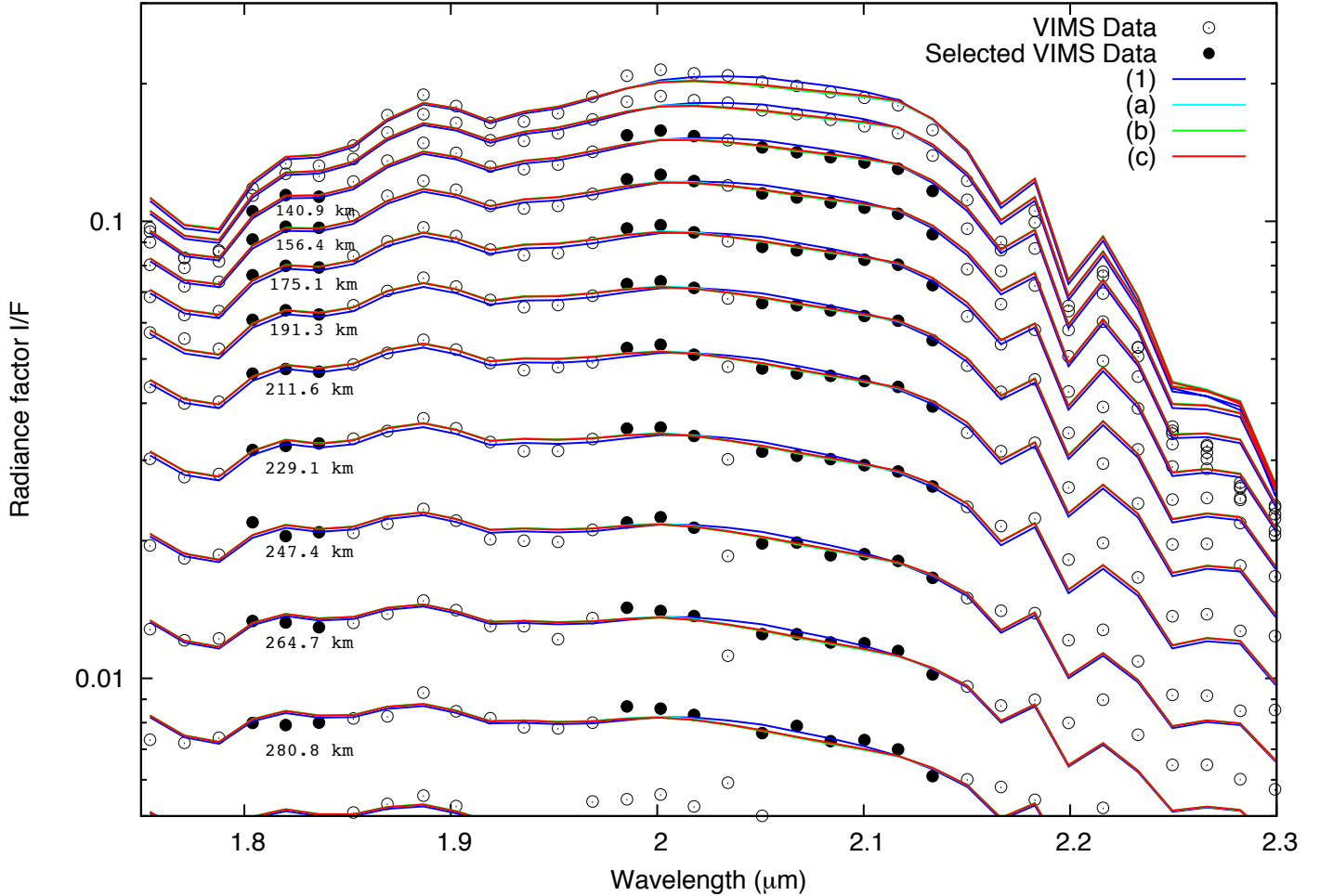


Fig. 7. As in Figure 4 except that model results are now overplot to data. Only the data shown with filled circles are actually used in our analysis and the retrievals. The spectra we used are labelled with their altitudes, from 140 to 280 km. The blue curve (labelled ①) corresponds to the results for the reference cut-off parameters and the curves labelled ②, ③ and ④ respectively correspond to cut-off parameters $\Delta\nu_{co} = 350 \text{ cm}^{-1}$ and $\gamma_{co} = 60 \text{ cm}^{-1}$, $\Delta\nu_{co} = 150 \text{ cm}^{-1}$ and $\gamma_{co} = 240 \text{ cm}^{-1}$ and $\Delta\nu_{co} = 13 \text{ cm}^{-1}$ and $\gamma_{co} = 360 \text{ cm}^{-1}$ taken in the zone of minimum χ^2 (see Figure 6). The curves labelled ②, ③ and ④ are extremely closed from each other and cannot be easily distinguished. Only data shown with a filled circle are used for the retrieval.

Table 1

Different natures for the absorption peak

Case	Nature of the peak	Remark
#1	Haze	Down to 80 km / No absorption below
#2	Gas with c^{ste} mixing ratio	All the column
#3	Condensable gas	Constant down to 60 km / No absorption below
#4	Haze and mist	All the column
#5	C_2H_6 GCM	From Rannou et al. (2006)
#6	CH_4	From Niemann et al. (2010)

window. It should be noted that for all these solutions, the amount of haze is the same within a relative interval of $\pm 6\%$ around an average value $F_H \simeq 2.17$. The root-mean square of the Gaussian absorption is around $0.02 \mu\text{m}$, but with γ_{co} around 0.012 for λ_0 around $2.05 \mu\text{m}$ and around 0.025 for λ_0 around $2.09 \mu\text{m}$.

It is not possible to compare directly the amplitude of the Gaussian function between different cases because

the absorption is added to different components and with different rules. Rather, we have to compare impact of these additional absorptions on the atmosphere's extinction properties. We then consider the extinction coefficients of the haze and the gas at 4 different altitudes in the atmosphere for the three cases of absorption peak along with the opacity of the haze and gas in a model without an additional peak. We are especially interested by the

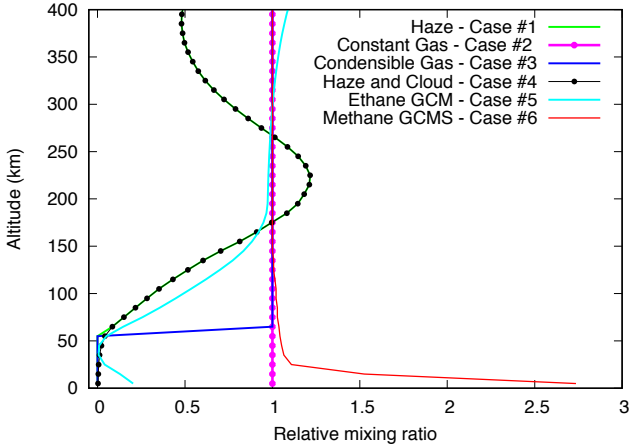


Fig. 8. Vertical profiles of the absorption peak fed into the model for the various cases studied in this work. Profiles are given as relative mixing ratio (only the shapes of the profiles matter) and the actual absorption is further scaled by a free parameter.

absorption peak that is needed with the reference cut-off values $\Delta\nu_{co} = 26 \text{ cm}^{-1}$ and $\gamma_{co} = 120 \text{ cm}^{-1}$. Then, if we could also use it at $2.0 \mu\text{m}$, all Titan’s spectra could be fitted with gaseous absorption treated in a consistent manner.

The prominence of the peak depends on the case we use to account for it. To obtain the same absorption feature in the scattered intensity we need an increasingly stronger peak if it is due to a non-condensable gas (case #2), to a condensable gas (case #3) or, finally, to the aerosol haze (case #1) (Figure 12). To understand this, we must note first that, in our model, the decrease in intensities in the $2 \mu\text{m}$ window is essentially produced by the influence of the multiple scattering due to the atmospheric column and not to the local optical properties of the atmosphere. This can be tested by setting the multiple scattering ratio $\rho_{ms}(z)$ to 1, without changing the atmosphere properties. Then, the intensity obviously decreases and the absorption feature around $\sim 2.07 \mu\text{m}$ completely disappears. This indicates that the absorption signature essentially comes from all layers through the multiple scattering and actually involves the entire atmospheric column.

In light of these results, we must consider how the absorption mechanisms of our three cases are consistent with sourcing from the entire column. For instance, the cases #2 and #3 differs only because the absorption feature exists respectively along all the atmosphere column or only above 60 km. As a consequence, the absorption must be more marked in the case #3 than in #2 to compensate for the smaller column. If the extinction peak is due to aerosols (case #1), then it has to be even stronger than for the gaseous cases. This is because the aerosol layer, in our model, goes down to 80 km and has a different vertical profile than methane (Figure 8). Below 80 km, haze is replaced by a mist which does not bear any absorption signature. Therefore, the way the absorption peak is attributed (to haze or to gaseous properties) and the vertical

distribution of the component which bears the absorption feature controls the depth of the absorbing layer.

To better understand the effect of the column depth on the absorption feature, we added three supplementary test cases for the vertical profile of the absorption feature. They represent variations around the previous cases. We only use these new profiles with the reference cut-off values $\Delta\nu_{co} = 26 \text{ cm}^{-1}$ and $\gamma_{co} = 120 \text{ cm}^{-1}$. We tested the case with an absorption feature borned by both the stratospheric haze above 80 km and mist below 80 km (case #4), the case of an absorption having a profile extracted from the 2D-IPSL Global Climate Model (IPSL GCM) for ethane (case #5) and the case of an absorption having a methane-like profile (case #6). We introduce this last case to perform a test on the optical depth of the column because the methane profile sharply increases below 40 km. But, since we are studying an absorption inside the methane window, we do not expect that this case may correspond to the reality. These profiles are given in Figure 8, along with the three former profiles. We generally find that a smaller peak is needed with a gaseous absorption than with a haze absorption (not shown here). We also find that a smaller absorption is needed when the vertical profile of absorption, whether it is due to haze or gas, goes deeper in the atmosphere. On the other hand, all these cases give statistically (in term of χ^2) the same fit of the scattered intensity. We conclude that observations of the scattering intensity at the limb are not sufficient and that we need to consider other observations in order to go further.

The Table 2 show the best peak parameters obtained for the reference cut-off, and for the six cases. Notably, the associated correlation matrices show that the four model parameters are well decorrelated since the highest non-diagonal term never exceed $3.5 \cdot 10^{-2}$. The center and the width of the absorption peak, λ_0 and Σ , that we retrieve appear consistent whatever is the source of absorption (i.e the case). Noteworthy, a more accurate value of λ_0 is approximately $2.065 \mu\text{m}$, with a maximum uncertainty ± 0.03 . We do not expect the amplitude of the peak A to be similar for the different cases because the absorption strength is defined relative to the absorption of the species which is assumed to bear the absorption. This absorption differs from case to case. Therefore, only the resultant extinctions (as in Figure 12), tangential opacities or transmissions through the atmosphere are relevant for comparison. This is the topic of the next section.

3.4. Occultations in the $2.0 \mu\text{m}$ window

To discriminate between the different solutions, we can compare the transmission at $2 \mu\text{m}$ window through a tangential line of sight at the limb of Titan produced by the different solutions with real occultation transmission (e.g., Bellucci et al., 2009; Maltagliati et al., 2015). None of the observations correspond to the latitude and the time period of the scattering observation. However, we also

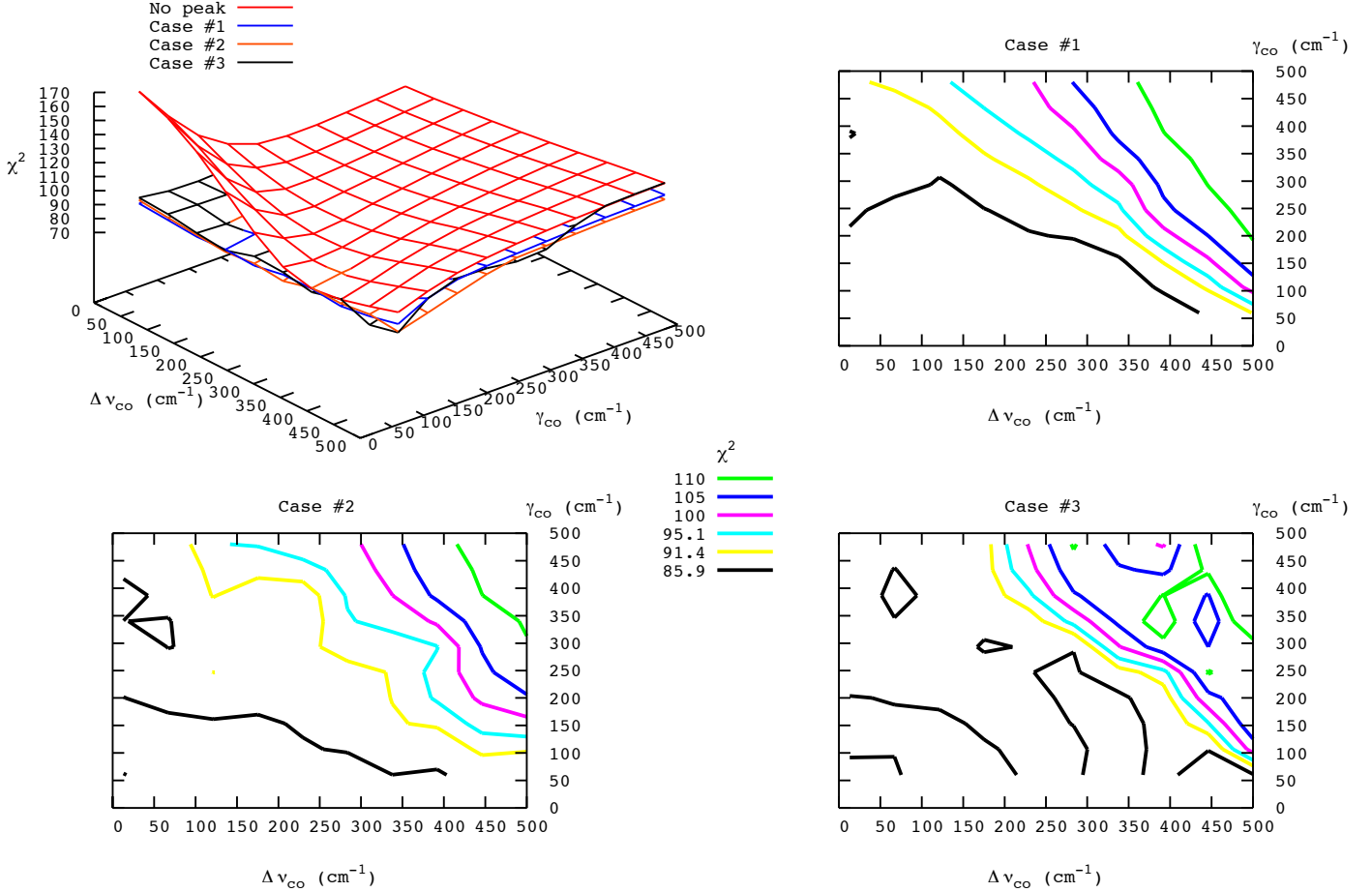


Fig. 9. (At top and left) Surfaces of χ^2 as a function of $\Delta\nu_{co}$ and γ_{co} . The χ^2 surface labelled *No peak* corresponds to the case already shown in Figure 6. The other surfaces show the χ^2 obtained with an absorption feature in the methane window. These maps show that the model results can be significantly improved if a supplementary absorption is included (case #1, #2 and #3). For the case of the reference cut-off values ($\Delta\nu_{co} = 26 \text{ cm}^{-1}$, $\gamma_{co} = 120 \text{ cm}^{-1}$), the match between data and model is the same as for the extended cut-off. The three cases give similar values of χ^2 , preventing us from preferring the fit of any one case. (At top and right) Same as Figure 6, and with the same χ^2 levels, but for the case #1 (the color code is displayed once for the three maps in the middle of the figure). The two levels $\chi^2 = 91.4$ (yellow) and $\chi^2 = 95.1$ (cyan) corresponds to the $1 - \sigma$ and $2 - \sigma$ error level. With these new simulations, the region where the fits fall below the 1 - or $2 - \sigma$ levels is much broader than in the case *No peak* and now includes the reference cut-off values. (At bottom, left and right) Same as Figure 6, for case #2 and #3.

Table 2

Best model parameters[†] for the reference cut-off[‡]

Case	λ_0	Σ	A	F_H
#1 (Haze)	$2.068^{+0.023}_{-0.023}$	$2.640^{+0.083}_{-0.075} \times 10^{-2}$	$3.759^{+0.055}_{-0.053} \times 10^{-2}$	$2.115^{+0.014}_{-0.014}$
#2 (Gas c ^{ste} mix. ratio)	$2.064^{+0.027}_{-0.027}$	$2.169^{+0.090}_{-0.078} \times 10^{-2}$	$4.143^{+0.130}_{-0.120}$	$2.114^{+0.014}_{-0.014}$
#3 (Condensable gas)	$2.062^{+0.023}_{-0.023}$	$2.074^{+0.081}_{-0.071} \times 10^{-2}$	$2.076^{+0.071}_{-0.063} \times 10^{+1}$	$2.115^{+0.014}_{-0.014}$
#4 (Haze and mist)	$2.068^{+0.024}_{-0.024}$	$2.681^{+0.086}_{-0.077} \times 10^{-2}$	$3.042^{+0.047}_{-0.044} \times 10^{-2}$	$2.116^{+0.014}_{-0.014}$
#5 (C ₂ H ₆ GCM)	$2.063^{+0.026}_{-0.026}$	$2.084^{+0.090}_{-0.078} \times 10^{-2}$	$1.569^{+0.041}_{-0.038} \times 10^{+1}$	$2.113^{+0.014}_{-0.014}$
#6 (CH ₄)	$2.068^{+0.031}_{-0.031}$	$2.485^{+0.110}_{-0.096} \times 10^{-2}$	$1.758^{+0.072}_{-0.062}$	$2.115^{+0.014}_{-0.014}$

[†] λ_0 , Σ and A describe the peak properties while F_H controls the amount of haze.

[‡] Reference profile cut-off values are $\Delta\nu_{co} = 26 \text{ cm}^{-1}$ and $\gamma_{co} = 120 \text{ cm}^{-1}$

remark that the relative difference between the transmission through the atmosphere at different altitudes $T(z)$ and the transmission of a synthetic continuum, $T_s(z)$, are very similar for all the observations. We then decided to use the four profiles to get the average value of the

$\Delta T(z)/T(z) = (T(z) - T_s(z))/T(z)$ and to evaluate the uncertainty on this value, including the intrinsic error of the observation (Maltagliati et al., 2015). For each observation, the synthetic continuum is assumed as a linear function computed from the value of transmission at

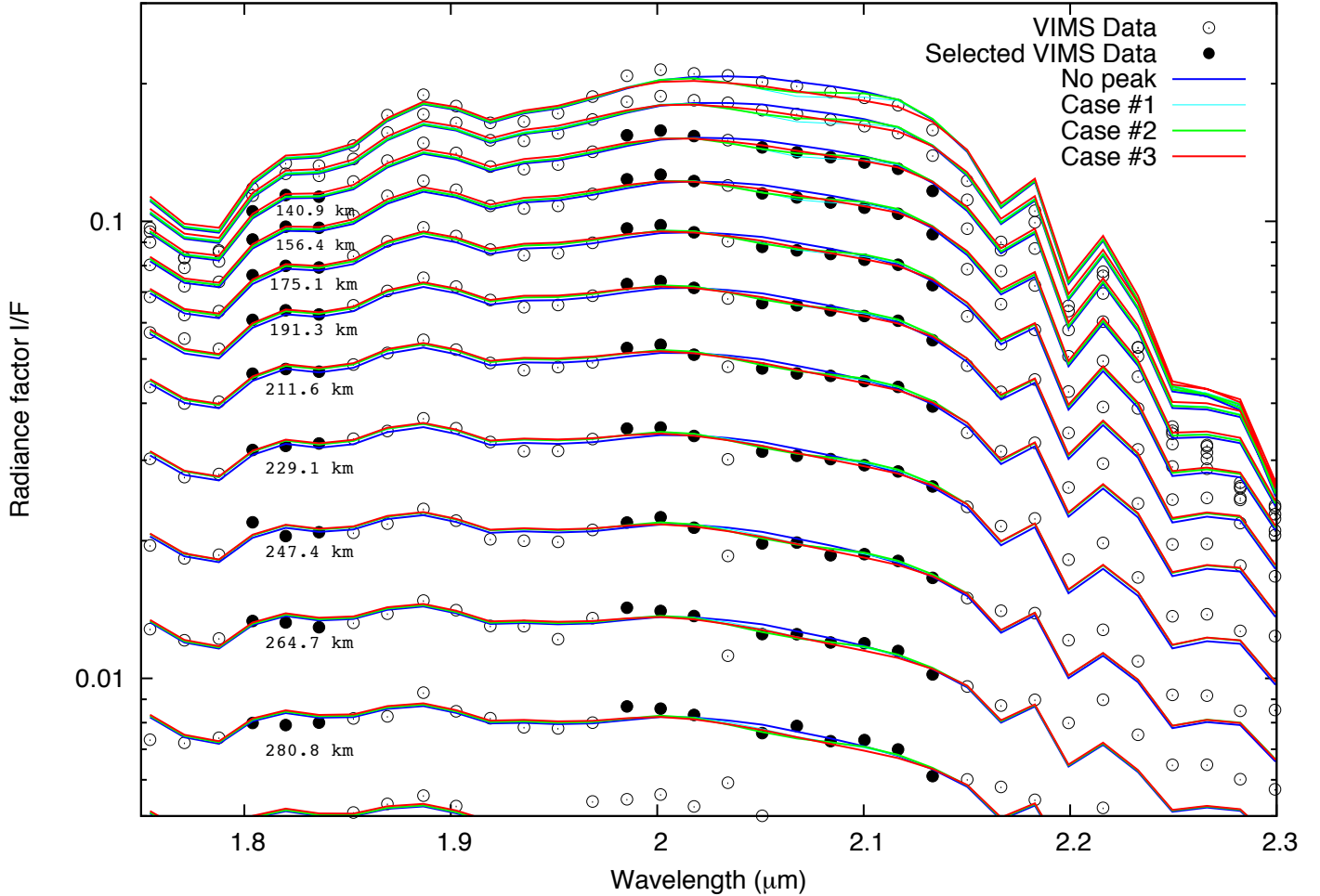


Fig. 10. As in Figure 7 except that we now overplot the results obtained for the reference cut-off values ($\Delta\nu_{co} = 25 \text{ cm}^{-1}$, $\gamma_{co} = 120 \text{ cm}^{-1}$), without peak (*No peak*) and with an absorption peak for case #1, case #2 and case #3. Only the data shown with filled circles are actually used in our analysis and the retrievals. The spectra we used are labelled with their altitudes, from 140 km to 280 km.

2.0 μm (channel #165) and at 2.1 μm (channel #171). In observations, the 2 μm window does not seem to have a noticeable absorption feature at 2.065 μm . We estimate that the potential dip in the transmission curve can not exceed 0.004 in term of transmission in the altitude range between 200 km and 300 km. This dip is barely perceptible in data while the various type of absorption profiles used in our model can yield more or less prominent peaks around 2.065 μm , depending on the case. For the case #1, #4, #3 and #5, we clearly see an absorption feature which exceeds the error level (Figure 13). These cases can be discarded. The case #6, only introduced for testing purpose, and the case #2 do not produce absorption feature in tangential transmission. These cases are those with the largest integrated column and, consequently, those that need the smallest absorption peak. Therefore, only the case #2 (a gas with constant mixing ratio) remains consistent with observations. Ethane has a tiny absorption feature inside the methane window, as already noted by Maltagliati et al. (2015), and could be a good candidate to explain this absorption feature.

The cross-sections of ethane as measured by Sharpe et al. (2004) give a set of spectroscopic structures between 2 and 2.05 μm : the Q-branch for the pure vibrational transitions and, at the sides of the Q-branch, the P and R-branches for the ro-vibrational lines. These measurements were performed at 5 $^{\circ}\text{C}$, 25 $^{\circ}\text{C}$ and 50 $^{\circ}\text{C}$, which is not representative of Titan's conditions. However, this is the only source of information that we have and the reader should realize that ethane cross-sections at Titan's temperature could be slightly different. The Q-branch matches quite well the sharp absorption in the channel #167, although possibly shifted by few nanometers. The absorption produced by the P-branch, at the large wavelength side of the central Q-branch, may explain the actual shape of the window. However, only a complete model using spectroscopic data of ethane accounting for the actual Titan's conditions could allow us to check if an absorption in the middle of the 2 μm could be explained by ethane. Notably, we used an *ad-hoc* Gaussian peak to mimic this absorption and we found its centre between 2.06 and 2.07 μm . But the real shape of the peak due to the P-branch is

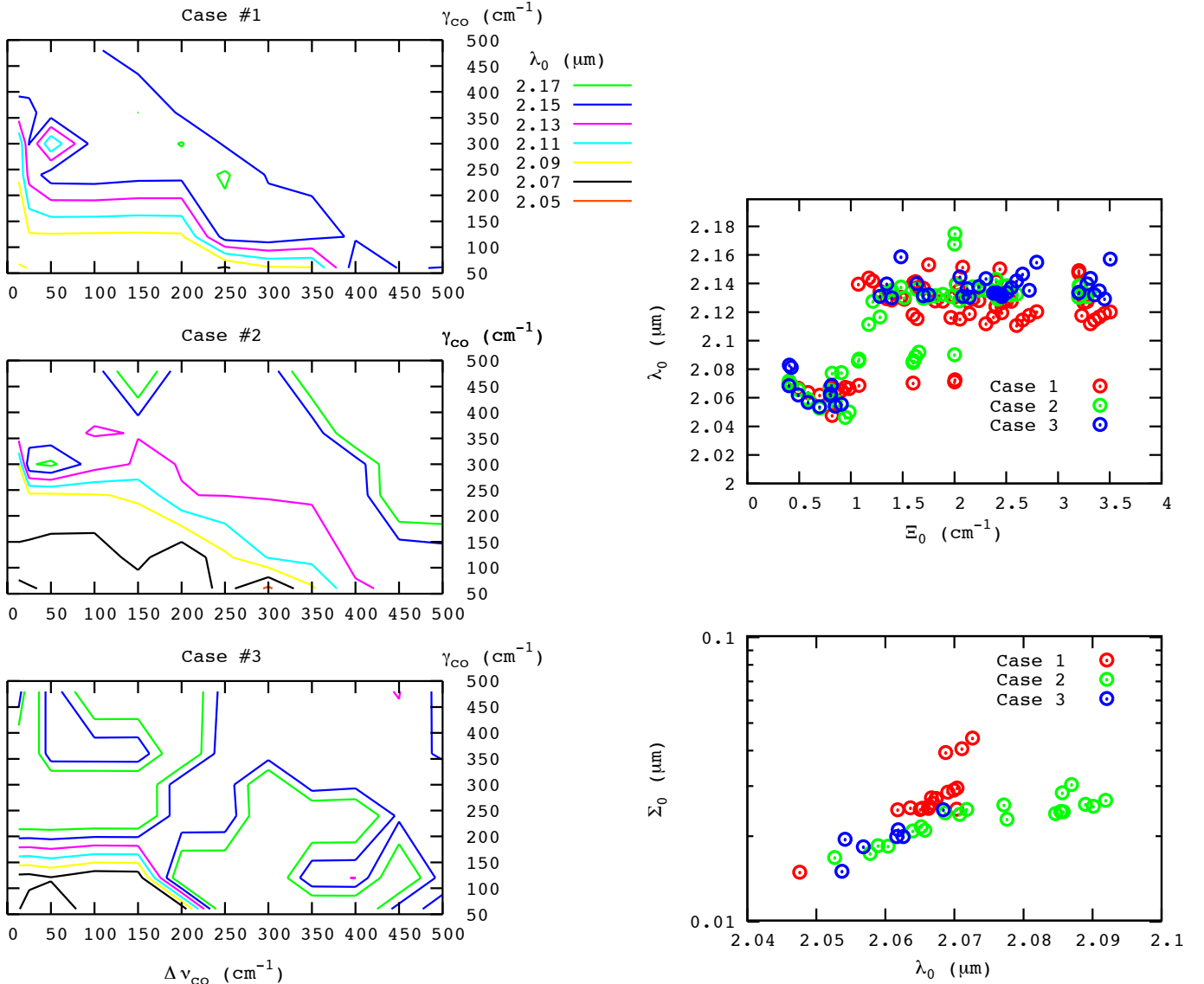


Fig. 11. At left : Maps of the absorption peak wavelength (λ_0) as a function of the $\Delta\nu_{co}$ and γ_{co} for the three cases of absorption (case #1, #2 and #3 from top to bottom). The color code is the same for the three graphs and is shown for the case #1 only. We can observe two distinct regions, with a peak between 2.05 and 2.08 μm at small values of $\Delta\nu_{co}$ and γ_{co} and another region at larger values of $\Delta\nu_{co}$ and γ_{co} with λ_0 larger than 2.10 μm . The transition between the two regions appears quite sharp. At right and top, the wavelength of the absorption peak λ_0 as a function of Ξ_{co} , defined as a metric in the $\Delta\nu_{co}$ and γ_{co} space as $\Xi_{co} = \sqrt{(\Delta\nu_{co}/150)^2 + (\gamma_{co}/350)^2}$. This graph clearly shows two populations of results, with λ_0 smaller than 2.1 μm for small values of Ξ_{co} (that is for cut-off applied close to the core of the lines) and another population with λ_0 beyond 2.1 μm for extended cut-off. At right and bottom, the standard deviation Σ_0 of the peak as a function of the peak wavelength λ_0 (only for values smaller than 2.1 μm) with the same color code as above.

asymmetrical with a peak slightly shifted toward short wavelengths and a longer tail toward large wavelengths. Finally, with spectroscopic data, we should also have an absorption feature at shorter wavelengths (due to the R-branch) around 2.01 μm . With an accurate treatment of ethane spectroscopy, one must expect absorption patterns able to modify the opacity in the methane 2 μm window.

It should be also noted that the GCMS onboard Huygens found a fairly constant mixing ratio for ethane with altitude, at the limit of the detection level (Niemann et al., 2010). However, the value appears quite uncertain in the low stratosphere and in the troposphere. The upper value

of ethane mixing ratio is given at $x_{\text{C}_2\text{H}_6} = 10^{-5}$ and, despite error bars are given and higher values may be found in some layers, the final result is given as an upper value. The GCMS also found a large quantity of several hydrocarbons and nitriles after Huygens landing. This revealed a wet surface with many condensing species, including ethane, in thermodynamical interaction with the atmosphere. We then expect the ethane mixing ratio to be different from 0, as assumed in the case #3 (condensable gas) or in simple models where condensable species are removed below a given altitude. This also contradicts somewhat the results of the 2D-IPSL GCM (input for case #5),

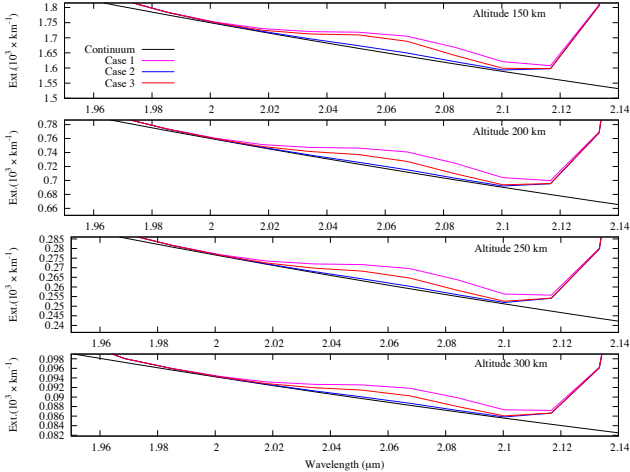


Fig. 12. Extinction of the atmosphere at four altitudes for the three cases (#1, #2 and #3), with the reference cut-off values ($\Delta\nu_{co} = 25 \text{ cm}^{-1}$, $\gamma_{co} = 120 \text{ cm}^{-1}$) along with the aerosols continuum. Although the three cases studied in this work gives comparable results for the scattered light at the limb, the corresponding extinctions appears very different and have more or less prominent absorption features.

which simulated Titan’s climate, cloud microphysics and interaction between condensable gas, droplets and aerosols. This model runs under some assumptions and approximations which could be revisited because they modify the vertical profile of ethane in the GCM. For instance, condensed methane and ethane on droplets are assumed to behave independently from each other. In reality, these condensed species, along with others, yield complex mixtures with thermodynamical laws differing from the laws of pure species. This would drastically modify the saturation vapor pressures above droplets and, more generally, it would provide more complex equilibrium conditions between condensed and gaseous phases.

The influence of the source of ethane at the surface is not included in the GCM, although it is now known that the surface at the Huygens landing site was rich in liquid ethane (Niemann et al., 2010) and that polar lakes also contain a fraction of liquid ethane as well (e.g., Brown et al., 2008). Such effects are not accounted for in the 2D-IPSL GCM and they could contribute in increasing the abundance of ethane in the troposphere especially near the sources at surface. We then assume that the best option to account for ethane in this present work is to assume a constant mixing ratio down to the surface, which corresponds to case #2.

4. Impact on the retrieval of the surface reflectivity

One important impact of having a good description of the opacity in the $2 \mu\text{m}$ is the ability to retrieve the surface reflectivity. Previous works based on photometry retrieved surface spectra which suggested that Titan’s surface could be made of water ice (Griffith et al., 2003;

Hirtzig et al., 2005; Rodriguez et al., 2006; Soderblom et al., 2009). The DISR instrument onboard Cassini observations yielded an *in situ* evaluation of the surface reflectivity spectrum (Tomasko et al., 2005; Schröder and Keller, 2008; Karkoschka et al., 2012; Karkoschka and Schröder, 2016). The surface spectra has a red slope from the visible to about $0.9 \mu\text{m}$, then a blue slope up to about $1.5 \mu\text{m}$, and finally a marked signature at $1.6 \mu\text{m}$, very similar to the water ice absorption signature. This spectra could be explained with a model of surface assuming a water ice layer covered by a mixture of aerosols and liquid (Rannou et al., 2016). This model also predicts the surface spectrum beyond $1.6 \mu\text{m}$, and suggests that the water ice should leave strong signatures. In the $2 \mu\text{m}$ window, the reflectivity should be seen as a U-shaped surface albedo, in the $2.8 \mu\text{m}$ window, the reflectivity should decrease continuously through the window and at $5 \mu\text{m}$, it should be relatively flat or slightly increasing.

The importance of describing the spectral behaviour of surface reflectivity inside each window, instead of discussing the window-averaged reflectivities, is that we would be able to constrain specific identifying signatures. This requires a fine knowledge of the opacities inside the window, or at least of its spectral behaviour. The $2.8 \mu\text{m}$ window is too poorly known to have a safe inversion because aerosol absorption has a strong variation across this window (Rannou et al., 2010) and several gaseous signatures shape this window. Ethane absorbs between 2.60 and $2.70 \mu\text{m}$ and beyond $2.8 \mu\text{m}$, as deuterated methane at $2.75 \mu\text{m}$, and possibly other gases further than $2.8 \mu\text{m}$. As mentioned previously, no ethane linelist is yet available for this wavelength range and the aerosol properties are very uncertain. Finally, the $5 \mu\text{m}$ window can be used to retrieve the surface albedo, but for water ice we expect a flat and featureless behaviour which will not give a strong clues. These arguments demonstrate the importance of understanding the $2 \mu\text{m}$ window: with better understood opacities, it can reveal a specific signature more reliably inverted than the $2.8 \mu\text{m}$ window.

To retrieve the surface albedo, we use an observation taken during the flyby of Titan T71. This is the same image as in Rannou et al. (2016), chosen because it has a moderate solar incidence ($\sim 35^\circ$) and emergence ($\sim 26^\circ$) angles and a fairly good spatial resolution (10 km) that allows to see quite homogeneous regions of dark and bright surfaces. This characteristics are fine for the purpose of the present study. We use two pixels, one taken in the bright zone and the other one in the dark zone. We accounted for a wavelength shift of 5.6 nm in the data recording of VIMS. In the model we strictly use the setup published by Doose et al. (2016) for the haze. We then use their vertical profile as a reference for both the haze and the mist. The spectral properties of haze and the gaseous absorption are computed in the same way has described for this study at the limb. We study $1.6 \mu\text{m}$ and $2.0 \mu\text{m}$ windows. For a given spectrum, we first use the intensity in the methane band to set the amount of haze and mist, scaling the refer-

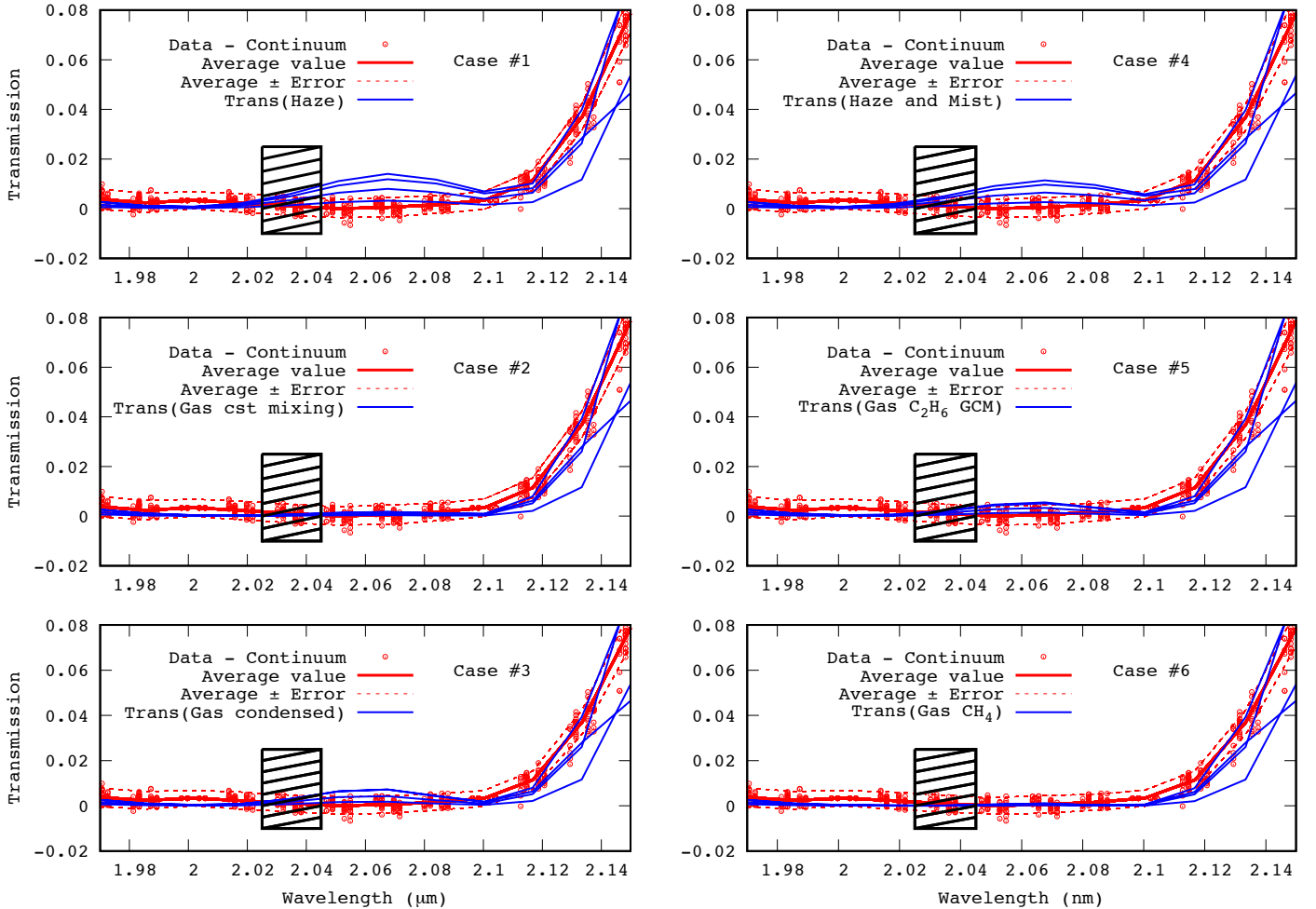


Fig. 13. Relative difference $((T - T_s)/T)$ between the transmission of the atmosphere (T) and the transmission of a synthetic haze continuum (T_s) as a function of the wavelength, in the range of altitude between 200 and 300 km, obtained from stellar occultation observed by VIMS (Maltagliati et al., 2015, , red lines and symbols). The rectangle with hatching represents a zone excluded from our analysis. The calculations for the model (blue lines) are obtained for the reference cut-off values $\Delta\nu_{co} = 26 \text{ cm}^{-1}$ and $\gamma_{co} = 120 \text{ cm}^{-1}$. The six figures correspond to the six cases of absorptions features, the three cases throughout this paper and the three additional cases (cf. Table 1). In these plots, an absorption inside the $2 \mu\text{m}$ window should appear as a peak around 2070 nm. The transmission computed by the model at four levels between 200 and 300 km (blue lines) may contain such a peak depending on the cases while data does not contain this peak.

ence vertical profile, with the factor F_H . Once the value of F_H is set, we used the complete spectrum to retrieve the surface reflectivities (A_i with $i = 1, N$) which remains the only free parameters. The index i runs over the number of channels which probes the surface. We use 13 different values : four values for the $1.6 \mu\text{m}$ window, and nine values for the $2 \mu\text{m}$ windows. These numbers of channels are essentially constrained by the spectral widths of these windows which give access to surface information.

We first retrieve the surface albedo without including absorption peak, but with different sets of cut-off parameters. Again we choose the reference values ($\Delta\nu_{co} = 26 \text{ cm}^{-1}$, $\gamma_{co} = 120 \text{ cm}^{-1}$) and cut-off parameters chosen in the region of minimum values of χ^2 (Figure 6): ($\Delta\nu_{co} = 100 \text{ cm}^{-1}$, $\gamma_{co} = 300 \text{ cm}^{-1}$), ($\Delta\nu_{co} = 150 \text{ cm}^{-1}$, $\gamma_{co} = 240 \text{ cm}^{-1}$) and ($\Delta\nu_{co} = 300 \text{ cm}^{-1}$, $\gamma_{co} = 120 \text{ cm}^{-1}$). As a result, we find a large difference between the retrieval obtained with the reference cut-off values, which give a de-

crease of the surface albedo with the wavelength, and the retrieval with extended cut-off which gives U-shaped surface spectra (Figure 14). The surface reflectivity retrieved with the reference set is very similar to previous results by Negrão et al. (2006, 2007) and Cours et al. (2010) for instance. Then, we now consider again the parameter set ($\Delta\nu_{co} = 26 \text{ cm}^{-1}$, $\gamma_{co} = 120 \text{ cm}^{-1}$) but, this time, with an absorption peak as in the case #2. We find that the retrieved surface albedo is flatter than in the reference case and do not produce a U-shape as the cases with extended cut-off. Adding a peak with the reference cut-off, as we do in this work, essentially modifies the surface albedo between 2.02 and 2.10 μm . Although the absorption feature is accounted for in a too simple way in this work, as discussed later, this demonstrates that the additional peak needed to explain the $2 \mu\text{m}$ window at the limb may also have an impact on the retrieved surface albedo.

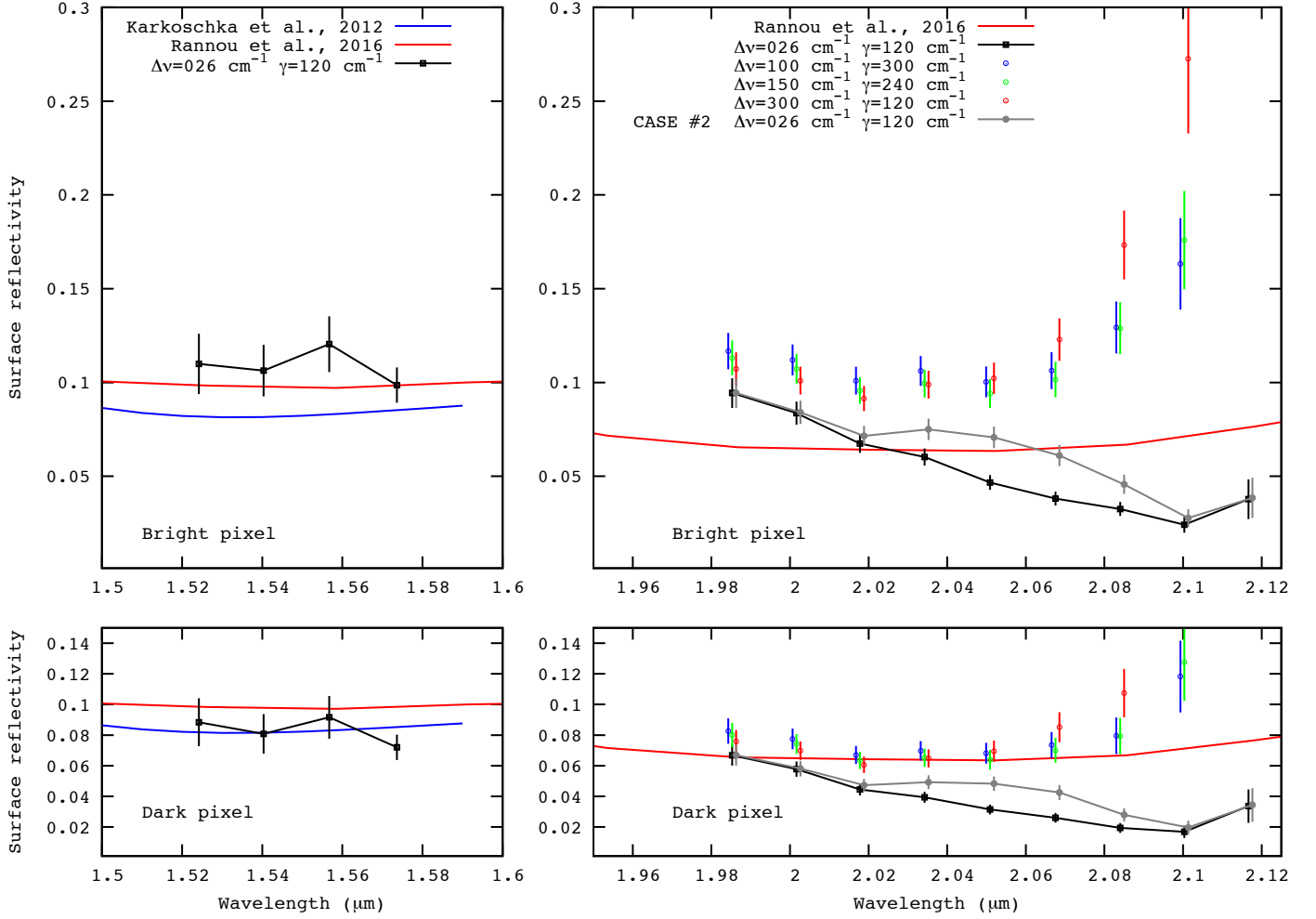


Fig. 14. Surface reflectivities observed by DISR (blue line), modelled with a surface model (red line) and retrieved in this work for a bright and black pixel in the 1.6 μm and 2.0 μm windows. The error bars are given to $1 - \sigma$. They essentially depends on the uncertainties on the radiance factor and on the uncertainty on the amount of haze. At 1.6 μm , we used the reference cut-off values for the retrieval (dark line). At 2.0 μm , we retrieved the surface reflectivity with different values of the cut-off parameters, the reference value and several extended values collected in region of low χ^2 reported in Figure 6, and no absorption peak. We also show the retrieved surface albedo obtained with the reference value of the cut-off parameters and with the absorption peak corresponding to the case #2.

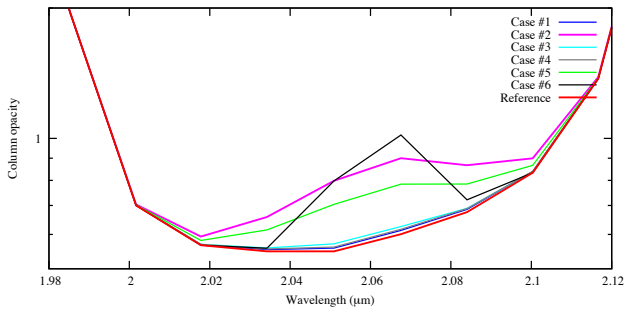


Fig. 15. Total column opacity of the atmosphere for the simulation that yielded the results displayed in Figure 14, for the reference cut-off values, and with the absorption cases #1 to #6.

5. Discussion and Conclusion

There are still some sources of uncertainties in our analysis that must be considered and could have potentially an impact on the result. We stress that this absorption peak,

presumably gaseous in nature, is represented by a Gaussian function, with an identical form at all altitudes, which may differ from a real gaseous absorption peak for at least three reasons. First, a gaseous peak essentially depends on the pressure level and on temperature which are not accounted for here. Secondly, if such an isolated absorption can produce a peak, its shape is probably not Gaussian. Finally, we excluded some spectral regions from our study where ethane is known to contribute to the absorption, however this gas may participate to the continuum absorption beyond this exclusion regions and also may alter the results. We know that the retrieval of the reflectivity is very sensitive to the total column opacity.

Despite these limitations, our results demonstrate that the 2 μm window can be fitted with the same line profile cut-off than other windows. For this, we need to include a supplementary peak of absorption at $2.065 \pm 0.027 \mu\text{m}$ (result for case #2 in Table 2). This absorption feature,

which appears clearly in the photometric observations at the limb, is treated in a *ad hoc* manner with a Gaussian absorption. This mimics a gaseous absorption, since an absorption by particles (haze or cloud) is clearly excluded by our analysis. Such a supplementary absorption has a consequence on the retrieved surface albedo. While the reference values for the line profile cut-off produces a monotonically decreasing reflectivity as already found in previous works, the absorption inside the 2 μm window modifies significantly the shape of the surface albedo. The result is difficult to examine in detail because the new retrieved surface albedo depends on the way the absorption peak is accounted for, and our procedure does not ensure an exact retrieval of the surface reflectivity. This result only shows that we have to expect a different surface spectrum at 2 μm when more accurate data will be available to treat ethane absorption (Viglaska et al., 2017).

We also note that using line profile cut-offs with larger extension, as those giving the minimum χ^2 in the initial test, may give satisfactory results. These parameters allow us to fit the limb photometry and the occultation quite well. Moreover, the surface reflectivity that we can retrieve with these parameters are higher and have a U-shape that would be expected for a water ice signature. However, this case alone would not explain the tiny absorption in the centre of the 2 μm window. Some solution including these extended cut-off and a supplementary absorption to produce a dip in the spectra of scattered light at the limb may also be considered. Although we can not exclude this solution, we think more likely that the line profile cut-off are similar at all windows, which favor the solution with the reference cut-off values and a peak as described in this work.

This work strongly suggests that ethane is responsible for this absorption. Although we removed the spectral intervals where ethane has its most prominent absorption features, we noticed a small absorption feature in the ethane absorption pattern at a wavelength larger than 2 μm , right in the centre of the window (Maltagliati et al., 2015). We found that to be consistent with both the observations of scattered light at the limb and the occultation, this absorption peak should be borne by an element following a constant mixing ratio, a characteristic of ethane (Niemann et al., 2010).

Acknowledgment:

This work has been performed thank to the Agence Nationale de la Recherche (ANR Project *APOSTIC* No. 11BS56002, France). The authors thank Dr S. MacKenzie for her helpful review and for significantly improve this paper.

References

References

Bailey J., Ahlsved L., Meadows V.S. **2011**. *The near-IR spectrum of*

- Titan modeled with an improved methane line list*. Icarus 213:218–32. doi:DOI: [10.1016/j.icarus.2011.02.009](https://doi.org/10.1016/j.icarus.2011.02.009). [arXiv:1102.2554](https://arxiv.org/abs/1102.2554).
- Barnes J.W., et al. **2007**. *Global-scale surface spectral variations on Titan seen from Cassini/VIMS*. Icarus 186:242–58. doi:DOI: [10.1016/j.icarus.2006.08.021](https://doi.org/10.1016/j.icarus.2006.08.021).
- Bellucci A., et al. **2009**. *Titan solar occultation observed by Cassini/VIMS: Gas absorption and constraints on aerosol composition*. Icarus 201:198–216. doi:DOI: [10.1016/j.icarus.2008.12.024](https://doi.org/10.1016/j.icarus.2008.12.024).
- Brown M.E., Bouchez A.H., Griffith C.A. **2002**. *Direct detection of variable tropospheric clouds near Titan’s south pole*. Nature 420:795–7. doi:DOI: [10.1038/nature01302](https://doi.org/10.1038/nature01302).
- Brown R.H., et al. **2008**. *The identification of liquid ethane in Titan’s Ontario Lacus*. Nature 454:607–10. doi:DOI: [10.1038/nature07100](https://doi.org/10.1038/nature07100).
- Clark R., Brown R., Lytle D. **2016**. *The VIMS Wavelength and Radiometric Calibration*. In: NASA Planetary Data System, The Planetary Atmospheres Node.
- Combes M., et al. **1997**. *Spatially Resolved Images of Titan by Means of Adaptive Optics*. Icarus 129:482–97. doi:DOI: [10.1006/icar.1997.5772](https://doi.org/10.1006/icar.1997.5772).
- Cours T., Rannou P., Coustenis A., Hamdouni A. **2010**. *A new analysis of the ESO Very Large Telescope (VLT) observations of Titan at 2 μm* . Planet Space Sci 58:1708–14. doi:DOI: [10.1016/j.pss.2009.12.009](https://doi.org/10.1016/j.pss.2009.12.009).
- Coustenis A., Lellouch E., Maillard J.P., McKay C.P. **1995**. *Titan’s surface: composition and variability from the near-infrared albedo*. Icarus 118:87–104. doi:DOI: [10.1006/icar.1995.1179](https://doi.org/10.1006/icar.1995.1179).
- Coustenis A., et al. **2001**. *Images of Titan at 1.3 and 1.6 μm with Adaptive Optics at the CFHT*. Icarus 154:501–15. doi:DOI: [10.1006/icar.2001.6643](https://doi.org/10.1006/icar.2001.6643).
- de Bergh C., et al. **2012**. *Applications of a new set of methane line parameters to the modeling of Titan’s spectrum in the 1.58 μm window*. Planet Space Sci 61:85–98. doi:DOI: [10.1016/j.pss.2011.05.003](https://doi.org/10.1016/j.pss.2011.05.003).
- Doose L.R., Karkoschka E., Tomasko M.G., Anderson C.M. **2016**. *Vertical structure and optical properties of Titan’s aerosols from radiance measurements made inside and outside the atmosphere*. Icarus 270:355–75. doi:DOI: [10.1016/j.icarus.2015.09.039](https://doi.org/10.1016/j.icarus.2015.09.039).
- Fedorova A., et al. **2015**. *The CO₂ continuum absorption in the 1.10- and 1.18- μm windows on Venus from Maxwell Montes transits by SPICAV IR onboard Venus express*. Planet Space Sci 113:66–77. doi:DOI: [10.1016/j.pss.2014.08.010](https://doi.org/10.1016/j.pss.2014.08.010).
- Fulchignoni M., et al. **2005**. *In situ measurements of the physical characteristics of Titan’s environment*. Nature 438:785–91. doi:DOI: [10.1038/nature04314](https://doi.org/10.1038/nature04314).
- Goody R., West R., Chen L., Crisp D. **1989**. *The correlated-k method for radiation calculations in nonhomogeneous atmospheres*. J Quant Spectrosc Radiat Transf 42:539–50. doi:DOI: [10.1016/0022-4073\(89\)90044-7](https://doi.org/10.1016/0022-4073(89)90044-7).
- Griffith C.A., Owen T., Wagener R. **1991**. *Titan’s surface and troposphere, investigated with ground-based, near-infrared observations*. Icarus 93:362–78. doi:DOI: [10.1016/0019-1035\(91\)90219-J](https://doi.org/10.1016/0019-1035(91)90219-J).
- Griffith C.A., Owen T., Miller G.A., Geballe T. **1998**. *Transient clouds in Titan’s lower atmosphere*. Nature 395:575–8. doi:DOI: [10.1038/26920](https://doi.org/10.1038/26920).
- Griffith C.A., Hall J.L., Geballe T.R. **2000**. *Detection of Daily Clouds on Titan*. Science 290:509–13. doi:DOI: [10.1126/science.290.5491.509](https://doi.org/10.1126/science.290.5491.509).
- Griffith C.A., et al. **2003**. *Evidence for the Exposure of Water Ice on Titan’s Surface*. Science 300:628–30. doi:DOI: [10.1126/science.1081897](https://doi.org/10.1126/science.1081897).
- Griffith C.A., et al. **2005**. *The Evolution of Titan’s Mid-Latitude Clouds*. Science 310:474–7. doi:DOI: [10.1126/science.1117702](https://doi.org/10.1126/science.1117702).
- Griffith C.A., et al. **2006**. *Evidence for a Polar Ethane Cloud on Titan*. Science 313:1620–2. doi:DOI: [10.1126/science.1128245](https://doi.org/10.1126/science.1128245).
- Griffith C.A., et al. **2012**. *Radiative transfer analyses of Titan’s tropical atmosphere*. Icarus 218:975–88. doi:DOI: [10.1016/j.icarus.2011.11.034](https://doi.org/10.1016/j.icarus.2011.11.034).
- Hanel R., Conrath B., Jennings D., Samuelson R. **2003**. *Exploration of the Solar System by Infrared Remote Sensing*. Cambridge University Press. ISBN:9780521818971.

- Hartmann J.M., et al. **2002**. *A far wing lineshape for H₂ broadened CH₄ infrared transitions*. J Quant Spectrosc Radiat Transf 72:117. doi:DOI: [10.1016/S0022-4073\(01\)00058-9](https://doi.org/10.1016/S0022-4073(01)00058-9).
- Hirtzig M., et al. **2005**. *Near-infrared study of Titan's resolved disk in spectro-imaging with CFHT/OASIS*. Planet Space Sci 53:535–56. doi:DOI: [10.1016/j.pss.2004.08.006](https://doi.org/10.1016/j.pss.2004.08.006).
- Hirtzig M., et al. **2009**. *A review of Titan's atmospheric phenomena*. Astron Astrophys Rev 17:105–47. doi:DOI: [10.1007/s00159-009-0018-0](https://doi.org/10.1007/s00159-009-0018-0).
- Hirtzig M., et al. **2013**. *Titan's surface and atmosphere from Cassini/VIMS data with updated methane opacity*. Icarus 226:470–86. doi:DOI: [10.1016/j.icarus.2013.05.033](https://doi.org/10.1016/j.icarus.2013.05.033).
- Karkoschka E., Tomasko M.G. **2010**. *Methane absorption coefficients for the jovian planets from laboratory, Huygens, and HST data*. Icarus 205:674–94. doi:DOI: [10.1016/j.icarus.2009.07.044](https://doi.org/10.1016/j.icarus.2009.07.044).
- Karkoschka E., Schröder S.E., Tomasko M.G., Keller H.U. **2012**. *The reflectivity spectrum and opposition effect of Titan's surface observed by Huygens' DISR spectrometers*. Planet Space Sci 60:342–55. doi:DOI: [10.1016/j.pss.2011.10.014](https://doi.org/10.1016/j.pss.2011.10.014).
- Karkoschka E., Schröder S.E. **2016**. *Eight-color maps of Titan's surface from spectroscopy with Huygens' DISR*. Icarus 270:260–71. doi:DOI: [10.1016/j.icarus.2015.06.010](https://doi.org/10.1016/j.icarus.2015.06.010).
- Khare B.N., et al. **1984**. *Optical constants of organic tholins produced in a simulated Titanian atmosphere - From soft X-ray to microwave frequencies*. Icarus 60:127–37. doi:DOI: [10.1016/0019-1035\(84\)90142-8](https://doi.org/10.1016/0019-1035(84)90142-8).
- Le Mouélic S., et al. **2012**. *Dissipation of Titan's north polar cloud at northern spring equinox*. Planet Space Sci 60:86–92. doi:DOI: [10.1016/j.pss.2011.04.006](https://doi.org/10.1016/j.pss.2011.04.006).
- Maltagliati L., et al. **2015**. *Titan's atmosphere as observed by Cassini/VIMS solar occultations: CH₄, CO and evidence for C₂H₆ absorption*. Icarus 248:1–24. doi:DOI: [10.1016/j.icarus.2014.10.004](https://doi.org/10.1016/j.icarus.2014.10.004). [arXiv:1405.6324](https://arxiv.org/abs/1405.6324).
- McKellar A.R.W. **1989**. *Low-temperature infrared absorption of gaseous N₂ and N₂ + H₂ in the 2.0-2.5 micron region - Application to the atmospheres of Titan and Triton*. Icarus 80:361–9. doi:DOI: [10.1016/0019-1035\(89\)90146-2](https://doi.org/10.1016/0019-1035(89)90146-2).
- Menard-Bourcin F., Menard J., Boursier C. **2007**. *Temperature dependence of rotational relaxation of methane in the 2 ν_3 vibrational state by self- and nitrogen-collisions and comparison with line broadening measurements*. Journal of Molecular Spectroscopy 242:55–63. doi:DOI: [10.1016/j.jms.2007.02.002](https://doi.org/10.1016/j.jms.2007.02.002).
- Negrão A., et al. **2006**. *Titan's surface albedo variations over a Titan season from near-infrared CFHT/FTS spectra*. Planet Space Sci 54:1225–46. doi:DOI: [10.1016/j.pss.2006.05.031](https://doi.org/10.1016/j.pss.2006.05.031).
- Negrão A., et al. **2007**. *The 2- μ m spectroscopy of Huygens probe landing site on Titan with Very Large Telescope/Nasmyth Adaptive Optics System Near-Infrared Imager and Spectrograph*. Journal of Geophysical Research (Planets) 112:E02S92. doi:DOI: [10.1029/2005JE002651](https://doi.org/10.1029/2005JE002651).
- Niemann H.B., et al. **2010**. *Composition of Titan's lower atmosphere and simple surface volatiles as measured by the Cassini-Huygens probe gas chromatograph mass spectrometer experiment*. Journal of Geophysical Research (Planets) 115(E14):E12006. doi:DOI: [10.1029/2010JE003659](https://doi.org/10.1029/2010JE003659).
- Rages K., Pollack J.B., Smith P.H. **1983**. *Size estimates of Titan's aerosols based on Voyager high-phase-angle images*. Journ Geoph Res 88:8721–8. doi:DOI: [10.1029/JA088iA11p08721](https://doi.org/10.1029/JA088iA11p08721).
- Rannou P., Cabane M., Botet R., Chassefière E. **1997**. *A new interpretation of scattered light measurements at Titan's limb*. Journ Geoph Res 102:10997–1014. doi:DOI: [10.1029/97JE00719](https://doi.org/10.1029/97JE00719).
- Rannou P., et al. **2006**. *Dust and cloud detection at the Mars limb with UV scattered sunlight with SPICAM*. Journal of Geophysical Research (Planets) 111:E09S10. doi:DOI: [10.1029/2006JE002693](https://doi.org/10.1029/2006JE002693).
- Rannou P., et al. **2010**. *Titan haze distribution and optical properties retrieved from recent observations*. Icarus 208:850–67. doi:DOI: [10.1016/j.icarus.2010.03.016](https://doi.org/10.1016/j.icarus.2010.03.016).
- Rannou P., et al. **2016**. *Titan's surface spectra at the Huygens landing site and Shangri-La*. Icarus 270:291–306. doi:DOI: [10.1016/j.icarus.2015.09.016](https://doi.org/10.1016/j.icarus.2015.09.016).
- Rey M., Nikitin A.V., Tyuterev V.G. **2013**. *Predictions for methane spectra from potential energy and dipole moment surfaces: Isotopic shifts and comparative study of ¹³CH₄ and ¹²CH₄*. Journal of Molecular Spectroscopy 291:85–97. doi:DOI: [10.1016/j.jms.2013.04.003](https://doi.org/10.1016/j.jms.2013.04.003).
- Rey M., et al. **2017**. *New accurate theoretical line lists of ¹²CH₄ and ¹³CH₄ in the 0-12000 cm⁻¹ range: application to the modeling of methane absorption in Titan's atmosphere*. Icarus .
- Rodriguez S., et al. **2006**. *Cassini/VIMS hyperspectral observations of the HUYGENS landing site on Titan*. Planetary and Space Sciences 54:1510–23. doi:DOI: [10.1016/j.pss.2006.06.016](https://doi.org/10.1016/j.pss.2006.06.016). [arXiv:0906.5476](https://arxiv.org/abs/0906.5476).
- Roe H.G., et al. **2005**. *Discovery of Temperate Latitude Clouds on Titan*. Astroph Journ Letters 618:L49–52. doi:DOI: [10.1086/427499](https://doi.org/10.1086/427499).
- Rothman L.S., et al. **2013**. *The HITRAN2012 molecular spectroscopic database*. J Quant Spectrosc Radiat Transf 130:4–50. doi:DOI: [10.1016/j.jqsrt.2013.07.002](https://doi.org/10.1016/j.jqsrt.2013.07.002).
- Schröder S.E., Keller H.U. **2008**. *The reflectance spectrum of Titan's surface at the Huygens landing site determined by the descent imager/spectral radiometer*. Planet Space Sci 56:753–69. doi:DOI: [10.1016/j.pss.2007.10.011](https://doi.org/10.1016/j.pss.2007.10.011). [arXiv:1702.00653](https://arxiv.org/abs/1702.00653).
- Sharpe S.W., et al. **2004**. *Gas-Phase Databases for Quantitative Infrared Spectroscopy*. Applied Spectroscopy 58:1452–61. doi:DOI: [10.1366/0003702042641281](https://doi.org/10.1366/0003702042641281).
- Smith P.H., et al. **1996**. *Titan's Surface, Revealed by HST Imaging*. Icarus 119:336–49. doi:DOI: [10.1006/icar.1996.0023](https://doi.org/10.1006/icar.1996.0023).
- Soderblom L.A., et al. **2009**. *The geology of Hotei Regio, Titan: Correlation of Cassini VIMS and RADAR*. Icarus 204:610–8. doi:DOI: [10.1016/j.icarus.2009.07.033](https://doi.org/10.1016/j.icarus.2009.07.033).
- Solomonidou A., et al. **2014**. *Surface albedo spectral properties of geologically interesting areas on Titan*. Journal of Geophysical Research (Planets) 119:1729–47. doi:DOI: [10.1002/2014JE004634](https://doi.org/10.1002/2014JE004634).
- Solomonidou A., et al. **2016**. *Temporal variations of Titan's surface with Cassini/VIMS*. Icarus 270:85–99. doi:DOI: [10.1016/j.icarus.2015.05.003](https://doi.org/10.1016/j.icarus.2015.05.003).
- Sromovsky L.A., et al. **2012**. *Comparison of line-by-line and band models of near-IR methane absorption applied to outer planet atmospheres*. Icarus 218:1–23. doi:DOI: [10.1016/j.icarus.2011.12.008](https://doi.org/10.1016/j.icarus.2011.12.008).
- Tomasko M.G., et al. **2005**. *Rain, winds and haze during the Huygens probe's descent to Titan's surface*. Nature 438:765–78. doi:DOI: [10.1038/nature04126](https://doi.org/10.1038/nature04126).
- Tomasko M.G., et al. **2008**. *A model of Titan's aerosols based on measurements made inside the atmosphere*. Planet Space Sci 56:669–707. doi:DOI: [10.1016/j.pss.2007.11.019](https://doi.org/10.1016/j.pss.2007.11.019).
- Viglaska D., Rey M., Nikitin A., Tyuterev V. **2017**. *Isotopic effects in infrared spectra via variational calculations: Reims-Tomsk approach for semirigid molecules and possible extensions*. In: Proceedings of the 25th Colloquium on High-Resolution Molecular Spectroscopy. p. 343.
- Vinatiev S., et al. **2010**. *Analysis of Cassini/CIRS limb spectra of Titan acquired during the nominal mission II: Aerosol extinction profiles in the 600-1420 cm⁻¹ spectral range*. Icarus 210:852–66. doi:DOI: [10.1016/j.icarus.2010.06.024](https://doi.org/10.1016/j.icarus.2010.06.024).
- Yurchenko S.N., Tennyson J. **2014**. *ExoMol line lists - IV. The rotation-vibration spectrum of methane up to 1500 K*. Monthly Notices of the Royal Astronomical Society 440:1649–61. doi:DOI: [10.1093/mnras/stu326](https://doi.org/10.1093/mnras/stu326). [arXiv:1401.4852](https://arxiv.org/abs/1401.4852).